

**THERMAL OXIDATION OF IRON OXIDE
NANOSHEETS IN THE PRESENCE OF
POTASSIUM IODIDE FOR CHROMIUM
REMOVAL**

TAN ZHEN SHENG

UNIVERSITI TUNKU ABDUL RAHMAN

**THERMAL OXIDATION OF IRON OXIDE NANOSHEETS IN THE
PRESENCE OF POTASSIUM IODIDE FOR CHROMIUM REMOVAL**

TAN ZHEN SHENG

**A project report submitted in partial fulfilment of the
requirements for the award of Bachelor of Engineering
(Honours) Mechanical Engineering**

**Lee Kong Chian Faculty of Engineering and Science
Universiti Tunku Abdul Rahman**

May 2022

DECLARATION

I hereby declare that this project report is based on my original work except for citations and quotations which have been duly acknowledged. I also declare that it has not been previously and concurrently submitted for any other degree or award at UTAR or other institutions.

Signature :



Name : Tan Zhen Sheng

ID No. : 17UEB02210

Date : 16/5/2022

APPROVAL FOR SUBMISSION

I certify that this project report entitled “**THERMAL OXIDATION OF IRON OXIDE NANOSHEETS IN THE PRESENCE OF POTASSIUM IODIDE FOR CHROMIUM REMOVAL**” was prepared by **TAN ZHEN SHENG** has met the required standard for submission in partial fulfilment of the requirements for the award of Bachelor of Engineering (Honours) Mechanical Engineering at Universiti Tunku Abdul Rahman.

Approved by,

Signature : *chaiy*

Supervisor : Dr. Ng Chai Yan

Date : 16/5/2022

The copyright of this report belongs to the author under the terms of the copyright Act 1987 as qualified by Intellectual Property Policy of Universiti Tunku Abdul Rahman. Due acknowledgement shall always be made of the use of any material contained in, or derived from, this report.

© 2022, Tan Zhen Sheng. All right reserved.

ACKNOWLEDGEMENTS

I would like to thank everyone who had contributed to the successful completion of this project. I would like to express my gratitude to my research supervisor, Dr. Ng Chai Yan for her invaluable advice, guidance and her enormous patience throughout the development of the research. Besides, I would like to express my appreciation to my senior, Soo Yew Hang who provides guidance and sharing of experiences in laboratory experimental works.

In addition, I would also like to express my gratitude to my loving parents and friends who had helped and given me encouragement. Without all the support from my supervisor, family, and friends, it is impossible for me to fulfil the tasks and complete the research successfully.

Last but not least, I would like to express my highest gratitude and appreciation to Universiti Tunku Abdul Rahman for the lab facilities and equipment provided to conduct the experimental works for research purposes.

ABSTRACT

Over the years, environmental pollution due to improper handling of Cr (VI) contaminant wastewater leads to high concerns from various researchers around the world. Up to date, Cr (VI) removal technique using nanomaterials is highly adopted due to the advantages of greater removal efficiency and cost-effectiveness. It is discovered that iron oxide nanostructures are favourable in removing Cr (VI) ions due to its strong magnetic properties. In this work, iron oxide nanosheets were produced by thermal oxidation with potassium iodide (KI). Sample characterisation tests of scanning electron microscopy (SEM), X-ray diffraction (XRD), and Cr (VI) removal analysis were conducted on the oxidised samples to determine the optimum oxidation temperature and duration to grow iron oxide nanosheets. SEM analysis showed that oxidation temperatures lower than the optimum temperature of 500 °C were insufficient to grow uniform and densely packed iron oxide nanosheets with high areal density. Besides, more obvious nanosheets with high areal density nanosheets were produced on the iron foil oxidised at the optimum duration of 2.5 h, which possessed the greatest average width and height with rather fine thickness. In XRD analysis, various oxides including hematite, magnetite, and potassium iron oxide (K_2FeO_4) as the dominant peak were identified on the samples oxidised with KI powder. Iron foil oxidised for optimum duration shows the highest intensities in overall, indicating that the sample was highly crystallised. Moreover, the Cr (VI) removal test conducted proved that the sample oxidised under optimum parameters achieved the best Cr (VI) removal efficiency of 83.22 % in 30 min as compared to those samples oxidised for other oxidation durations. This could be attributed to better morphological and structural properties possessed by the best sample which provided larger surface area for more sites to undergo electrostatic reaction with Cr (VI) ions. It was also justified that the presence of KI powder in the oxidation of iron foil enhanced the Cr (VI) removal efficiency.

TABLE OF CONTENTS

DECLARATION		i
APPROVAL FOR SUBMISSION		ii
ACKNOWLEDGEMENTS		iv
ABSTRACT		v
TABLE OF CONTENTS		vi
LIST OF TABLES		ix
LIST OF FIGURES		x
LIST OF SYMBOLS / ABBREVIATIONS		xii
 CHAPTER		
1	INTRODUCTION	1
	1.1 General Introduction	1
	1.2 Importance of the Study	2
	1.3 Problem Statement	3
	1.4 Aim and Objectives	4
	1.5 Scope and Limitation of the Study	4
	1.6 Contribution of the Study	5
	1.7 Outline of the Report	5
2	LITERATURE REVIEW	6
	2.1 Introduction	6
	2.2 Heavy Metal: Chromium and Its Application in Various Industries	6
	2.2.1 Impacts of Chromium (VI) on the Environment	8
	2.2.2 Background of Chromium Removal Process: Iron Oxide as Cr (VI) Absorbent	9
	2.3 Introduction of Iron Oxides	11
	2.3.1 Crystal Structures of Various Iron Oxides	11

	2.3.2 Basic Properties of Iron Oxides	15
2.4	Iron Oxide Nanostructures	16
	2.4.1 One-Dimensional Iron Oxide Nanostructures	16
	2.4.2 Synthesis of Iron Oxide Nanowires	17
	2.4.3 Growth Mechanism: Iron Oxide Nanostructures Grown by Thermal Oxidation	20
2.5	Thermal Oxidation	21
	2.5.1 Background of Thermal Oxidation for the Synthesis of α -Fe ₂ O ₃ Nanowires	23
	2.5.2 Effect of Thermal Oxidation Parameters on the Iron Oxide Nanostructures	26
	2.5.3 Thermal Oxidation with Potassium Halides	29
2.6	Summary of Literature Review	31
3	METHODOLOGY AND WORK PLAN	33
	3.1 Introduction	33
	3.2 Material for Experiments	33
	3.3 Thermal Oxidation Process	34
	3.4 Experimental Characterisation Tests	35
	3.4.1 Morphological Analysis	35
	3.4.2 Structural Analysis	36
	3.4.3 Chromium (VI) Removal Test and Analysis	37
	3.5 Summary	41
4	RESULTS AND DISCUSSION	42
	4.1 Introduction	42
	4.2 Morphological Analysis: Scanning Electron Microscopy (SEM)	42
	4.2.1 The Effect of Oxidation Temperature on the Growth of Iron Oxides	42
	4.2.2 The Effect of the Oxidation Duration on the Growth of Iron Oxides	44

4.2.3	The Effect of the Presence of Potassium Iodide in Thermal Oxidation on the Growth of Iron Oxide	50
4.3	Structural Analysis: X-Ray Diffraction (XRD)	52
4.4	Chromium (VI) Removal Analysis	55
4.5	Summary	57
5	CONCLUSIONS AND RECOMMENDATIONS	59
5.1	Conclusions	59
5.2	Recommendations for future work	60
	REFERENCES	61

LIST OF TABLES

Table 2.1:	Summarised Literature Review on Iron Oxide Nanostructures Synthesised via Thermal Oxidation.	24
Table 3.1:	List of Experimental Materials.	34
Table 4.1:	Dimensions of Nanosheets Formed on the Samples Oxidised at 500 °C for Different Duration.	46
Table 4.2:	The Heights of Nanosheets Formed on the Oxide Layer of the Samples Oxidised at 500 °C for 1.5, 2, 2.5, and 3 h.	50

LIST OF FIGURES

Figure 2.1:	Oxygen in the HCP Structure with Cations Distributed in Octahedral Interstices (Cornell and Schwertmann, 2003).	12
Figure 2.2:	Distribution of Iron Ions Over Oxygen Layer and Octahedral Hexagonal Arrangement (Cornell and Schwertmann, 2003).	12
Figure 2.3:	Octahedra Arrangement (Cornell and Schwertmann, 2003).	13
Figure 2.4:	Structure of Magnetite (Fe_3O_4): (a) Polyhedral model, (b) Ball-stick Model, and (c) Octahedra and Tetrahedral Ball-stick Model (Cornell and Schwertmann, 2003).	14
Figure 2.5:	(a) Octahedral Arrangement of Wüstite and (b) Ball-stick Model of Wüstite (Cornell and Schwertmann, 2003).	15
Figure 2.6:	Schematics of 1-D Nanostructures: (a) Nanorod, (b) Nanowire, (c) Nanoneedle, and (d) Nanotube (Lockman, 2018).	17
Figure 2.7:	Images of Nanowires Obtained from FESEM: (a) 300 °C (Water Vapour), (b) 400 °C (Water Vapour), (c) 400 °C (Dry Air), (d) 500 °C (Water Vapour), and (e) 500 °C (Dry Air) (Budiman et al., 2016a).	19
Figure 2.8:	FESEM Magnification Images of Nanowires at 400°C in Water Vapour (Budiman et al., 2016a).	19
Figure 2.9:	Mass Transport Mechanism of Iron Ions for Growth of Iron Oxide (a) Nanowire and (b) Nanobelt (Aquino et al., 2018).	21
Figure 2.10:	SEM Images of Iron Oxidised at 500 °C for 2 h (Budiman et al., 2016a).	22
Figure 2.11:	Cross Section of Iron Oxide Nanostructures at (a) 400 °C and (b) 600 °C of Oxidation Temperature (Yuan et al., 2012a).	26
Figure 2.12:	XRD Patterns of Iron Oxide Sheets Formed at Different Temperatures (Grigorescu et al., 2012).	28
Figure 2.13:	Nanowires Formed at the Part Deposited with Potassium Halide Grains (Qi, Wang and Liu, 2003).	31

Figure 3.1:	Muffle Furnace.	35
Figure 3.2:	Scanning Electron Microscope (Hitachi S-3400N).	36
Figure 3.3:	X-ray Diffractometer.	36
Figure 3.4:	100 mg/L (left) and 10 mg/L (right) of Cr (VI) Solution Prepared in Volumetric Flasks.	37
Figure 3.5:	pH Indicator Paper Used to Identify the Acidity of the Solution.	38
Figure 3.6:	Conical Flasks Shaken in the Incubator Shaker.	39
Figure 3.7:	Aliquot Solution Sample Mixed with 35 μ L of 1,5-diphenyl-carbazide Solution in the Centrifugal Tube.	40
Figure 3.8:	Aliquot Sample with Spectroscopy Blank in Plastic Cuvette for Ultraviolet-visible Spectrophotometry Analysis.	40
Figure 3.9:	UV-VIS Spectrophotometer.	41
Figure 4.1:	SEM Images of Iron Oxide Synthesised by Different Oxidation Temperatures for 2 h: (a) 200, (b) 300, (c) 400, and (d) 500 $^{\circ}$ C.	43
Figure 4.2:	SEM Images of Iron Oxide Nanostructures Synthesised at 500 $^{\circ}$ C for Different Oxidation Time: (a) 0.5, (b) 1, (c) 1.5, (d) 2, (e) 2.5, and (f) 3 h.	45
Figure 4.3:	The Cross Sectional SEM Images Tilted 45 $^{\circ}$ of the Iron Foil Oxidised at 500 $^{\circ}$ C for (a) 1.5, (b) 2, (c) 2.5, and (d) 3 h.	49
Figure 4.4:	SEM Images of Iron Oxide Nanostructures Formed by Thermal Oxidation at 500 $^{\circ}$ C for 2 h: (a) With and (b) Without KI Powder.	51
Figure 4.5:	XRD Patterns of Bare Fe Foil, Iron Foils Oxidised with KI Powder at 500 $^{\circ}$ C for Duration of 0.5, 1, 1.5, 2, 2.5, and 3 h, and the Iron Foil Oxidised at 500 $^{\circ}$ C for 2 h Without KI powder.	53
Figure 4.6:	Cr (VI) Removal Efficiency of Bare Fe Foil, Iron Foils Oxidised with KI Powder at 500 $^{\circ}$ C for Duration of 0.5, 1, 1.5, 2, 2.5, and 3 h, and the Iron Foil Oxidised at 500 $^{\circ}$ C for 2 h Without KI Powder in 30 min.	56

LIST OF SYMBOLS / ABBREVIATIONS

e^-	electron
h^+	hydrogen ion
E^0	reduction potentials
M_s	saturation magnetisation, emu.g ⁻¹
α	homogeneous void fraction
SEM	scanning electron microscopy
FESEM	field emission scanning electron microscopy
XRD	X-ray diffraction
HCP	hexagonal closely packed
FCC	face-centered cubic
D	dimensional
Ppm	parts per million

CHAPTER 1

INTRODUCTION

1.1 General Introduction

Over the years, the rapid growth of industrial sectors around the world has raised serious concerns in society regarding the issues of the disposal of heavy metals and corresponding pollution. Chromium as one of the heavy metals, its solubility, mobility and responsiveness in the form of Cr (VI) severely harms the environment. Cr (VI) is classified as a human carcinogen which can be an allergen to humans (Ukhurebor et al., 2021). Thus, several methods were identified to remove Cr (VI) ions from the chromium-contaminant wastewater, including chromium absorption, electrochemical treatment, chemical precipitation, and ion-exchange technologies (Sawada et al., 2004; Galán, Castañeda and Ortiz, 2005; Burks et al., 2014). According to Rafatullah et al. (2010), chromium absorption is found to be a better method due to the greater efficiency and cost-effectiveness in removing Cr (VI) from polluted water. In this work, iron oxide nanosheets are selected as the absorbent material for chromium removal.

Iron generally exists in different forms of oxides including hematite (α -Fe₂O₃), magnetite (Fe₃O₄), and maghemite (γ -Fe₂O₃). Mostly, iron oxides exist in divalent and trivalent state with their ions, Fe²⁺ and Fe³⁺ respectively. These oxides consist of closely packed oxygen molecules where octahedral and tetrahedral cavities partially bond with Fe²⁺ and Fe³⁺ ions (Suman et al., 2021). Iron oxide nanostructures have successfully gained the interest of various researchers due to their characteristics such as controllable size, low toxicity, strong magnetic properties, and lastly high surface area allowing them to be used widely for sustainable energy consumption and pollution control (Ashraf et al., 2020). Iron oxide as the positively charged absorbent is able to remove Cr (VI) ions from wastewater due to its specific amphoteric properties (Budiman et al., 2016a). Iron oxide nanosheets in the nanoscale increase the surface contact area for the absorption process, thus the chromium absorption performance is expected to be increased.

Thermal oxidation is known as one of the most favourable methods to synthesise iron oxide nanostructures due to the advantages of rapid production of nanostructures material on a large scale without requiring toxic and hazardous chemicals (Zhao et al., 2013). This process involves direct heating onto the bulk metals with the presence of oxygen at temperatures between 400 °C and 800 °C. When the iron is oxidised at a relatively high temperature, the atoms are having higher kinetic energy and the oxide film will continue to grow and thicken from the surface of the bulk metal iron. The iron grows on a scale of various phased oxides with hematite (α -Fe₂O₃) grown at the outer layer (Budiman et al., 2016b). Recently, various studies on the thermal oxidation of iron under different atmosphere such as oxidation in dry oxidising air, water vapour, etc. have been conducted by researchers. However, it is found that there are only a few studies conducted regarding the thermal oxidation of metals with potassium halides.

It is reported that the presence of potassium halides in thermal oxidation enhances the growth of metal oxide nanostructures. A similar study had been proposed by Qi, Wang and Liu (2003) in the preparation of tungsten oxide nanowires by thermal oxidation with potassium iodide powder. This synthesis technique is expected to be implemented in the synthesis of highly oriented nanowires or nanosheets of other metals. Thus, in this work, the study on the synthesis of iron oxide nanosheets through thermal oxidation with potassium iodide was conducted. The synthesis process is not only simple but also effective in producing large scale of nanostructures rapidly. Then the produced oxide nanosheets are tested to remove Cr (VI) in the absorption process and the respective absorption efficiency is determined. The thermal oxidation of iron with potassium iodide is conducted at the temperature of 200-500 °C at 5 °C/min of heating rate for 2 h. The sample with the best surface morphology is then proceeded with oxidation for 0.5, 1.0, 1.5, 2, 2.5, and 3 h, respectively to identify the optimum oxidation temperature and duration.

1.2 Importance of the Study

Due to the rapid development in the industrial sectors, the issues regarding the pollution of hexavalent chromium have continuously gained serious

concerns which have led to the necessary studies for various chromium removal techniques. Ineffective treatment of the industrial wastes is discharged into the water systems and transferred to the food chains, thus harming the natural environment and marine life (Aigbe and Osibote, 2020). Besides, there are hundred thousands of workers estimated to be potentially exposed to wastewater containing Cr (VI) which might be suffering from severe health issues such as lung cancer (Shanker and Venkateswarlu, 2019). Currently, achieving complete removal of chromium ions is difficult using alkali traditional precipitation since chromium complexes are stable and highly soluble across a wide pH range (Feng et al., 2021). Therefore, to overcome the problems mentioned above, research on the chromium removal by absorption using nanomaterials is necessary needed.

1.3 Problem Statement

Thermal oxidation process is known as one of the most effective methods to synthesise iron oxide nanostructures due to simple and easy setup and experimental procedures. Recent researches on the iron oxide nanostructures formed by thermal oxidation under oxygen and water vapour were conducted, and the results proved that denser and more uniform nanowires and nanosheets were produced under water vapour which enhanced the chromium absorption efficiency (Budiman et al., 2016a). However, it is found that there are limited research topics revealing the formation of iron oxide nanostructures with potassium halides via thermal oxidation. According to the study conducted by Qi, Wang and Liu (2003), highly oriented potassium-doped tungsten oxide nanowires were successfully produced and it is expected to be able to implement similar synthesis techniques in the growth of iron oxide nanostructures. Therefore, it is desirable for this project to conduct the experiment of thermal oxidation with potassium iodide for the growth of iron oxide nanosheets and investigate optimum experimental parameters including the oxidation environment, temperature, and time.

1.4 Aim and Objectives

This project is aimed to synthesise the iron oxide nanosheets through thermal oxidation for chromium removal. There are total three objectives listed below in order to accomplish the aim of the research:

- i. To determine the optimum thermal oxidation temperature and growth time for the iron oxide nanosheets synthesised with the aid of potassium iodide.
- ii. To examine the morphological and structural properties of the iron oxide nanosheets.
- iii. To identify the relationship of the surface morphology and structural properties of iron oxide nanosheets with chromium removal efficiency.

1.5 Scope and Limitation of the Study

This topic of research covered the synthesis of iron oxide nanosheets by thermal oxidation in the presence of potassium iodide for Cr (VI) removal. The parameters for the thermal oxidation process (oxidation temperature, time, and oxidation of iron with potassium iodide) were altered to observe and investigate the morphology of nanostructures produced. Different surface morphology of iron oxide was expected to directly affect the respective efficiency of Cr (VI) removal. The scope of this study includes a series of sample characterisation tests conducted to investigate the iron oxide nanosheets synthesised. The surface morphology of the iron oxide produced was investigated using SEM analysis. Next, the crystal structure and oxide phases found on iron oxide nanostructures were determined by XRD. Lastly, the chromium removal test was conducted to study the Cr (VI) removal efficiency of the specimens produced.

However, this research only covered a few parameters in the thermal oxidation process including the temperature, time, and the effect of potassium iodide on the growth of iron oxide nanostructures. Other factors such as oxidising pressure and concentration of oxygen, were not investigated. Another limitation is that the temperature of thermal oxidation in this work should be lower than the melting point of potassium iodide (KI). In short, this

study investigated the optimum oxidation temperature and time for the growth of iron oxide nanostructures with potassium iodide.

1.6 Contribution of the Study

In this study, the success of producing iron oxide nanosheets by thermal oxidation of iron foil covered with potassium iodide powder in air was proven. The optimum oxidation parameters of temperature and duration were identified based on the morphological, structural, and Cr (VI) removal analysis. The study further proposed that potassium-compound such as KI is essential and effective in enhancing the growth of iron oxide nanosheets due to the simple synthesis process. In addition, iron oxide as the low cost and abundant absorbent material is highly suggested for Cr (VI) ion removal.

1.7 Outline of the Report

This research report mainly consists of five chapters, each chapter contains several sub-sections. First, Chapter 1 is the introduction of the research, which consists of general introduction, significance of the study, and problem statement. Besides, the aim and objectives, scope and limitation, and contribution of the study are covered as well as the outline of the report.

Next, Chapter 2 is mainly describing the literature review of the study, which covers the sub-sections of introduction, heavy metal: chromium and its application in various industries, introduction to iron oxides, iron oxide nanostructures, iron oxide nanowires synthesis, process of thermal oxidation, and summary of literature review.

Moreover, Chapter 3 covers the research methodology and work plan, which involves material preparation and thermal oxidation process as well as the morphological, structural, and Cr (VI) removal analyses. Meanwhile, Chapter 4 outlines the result and discussion which analysed and discussed the iron oxides synthesised under various oxidation parameters by the verification of sample characterisation tests.

In conclusion, Chapter 5 describes the conclusion of the research and future recommendations to be implemented in future works.

CHAPTER 2

LITERATURE REVIEW

2.1 Introduction

The latest research about heavy metal chromium and the background of the removal process are firstly reviewed in this chapter. Next, a comprehensive review of iron oxide and its basic properties is discussed. In addition, iron oxide in the form of nanostructures is reviewed and lastly, the study on the thermal oxidation for iron oxide nanostructures synthesis is conducted.

2.2 Heavy Metal: Chromium and Its Application in Various Industries

Heavy metals are those metallic elements that are dangerous or fatal even in only small amount of quantities (Chew et al., 2019). Chew et al. (2019) further claimed that these metallic elements including chromium (Cr), lead (Pb), silver (Ag), zinc (Zn), nickel (Ni), mercury (Hg), and arsenic (As), are found to be one of the major contaminants to the water resources such as rivers and oceans and they have a minimum density which at least five times denser than the water. Currently, the aquatic environment including most of the water resources is continuously loaded with contaminants due to the existence of heavy metals from the developing industries (Budiman et al., 2016a).

Chromium, with the chemical element symbol Cr, is one of the most common heavy metals used in the industry. Chromium as a hard transition metal is steely-grey in colour and can be found naturally inside the crust of the earth as chromite ore (FeCr_2O_4) (Sharma et al., 2021). Most of the time it is found in the state of trivalent chromium, Cr (III) in nature. In the periodic table of elements, it belongs to the first element of the d-block, group (VI). According to Ukhurebor et al. (2021), the basic properties of chromium consist of an atomic number of 24, its atomic mass is 51.996 g/mol, and the density of chromium is 7.19 gcm^3 . Also, chromium reaches its melting point at 1907 °C and boiling point at 2672 °C (Aigbe and Osibote, 2020). Chromium exists in several states, forming its ions from Cr (II) to Cr (VI),

which are also known as Cr^{2+} and Cr^{6+} , respectively (Sharma et al., 2021). Among the different forms of chromium ions, Cr (III) and Cr (VI) are the most commonly found and both are highly stable as compared to other states of ions. Cr (III) is claimed to be less noxious and mobile as compared to Cr (VI) in terms of toxicity (Aigbe and Osibote, 2020). Cr (VI) carries an oxidising effect and also provides free radicals to prevent depletion of Cr (VI) to Cr (III) (Kerur et al., 2021). Cr (VI) is a hundredfold more virulent than Cr (III). It is hydrophilic in nature, water affinitive, and ready to be reduced, as claimed by Kerur et al. (2021). In aqueous solutions, Cr (VI) occurs in various species, mostly in the form of chromate, such as CrO_4^{2-} , $\text{Cr}(\text{OH})^{2+}$, $\text{Cr}(\text{OH})_3$ and $\text{Cr}(\text{OH})_4^-$; and dichromate including $\text{Cr}_2\text{O}_7^{2-}$, HCrO_4^- , and CrO_4^{2-} (Aigbe and Osibote, 2020).

Budiman et al. (2016b) states that chromium has been used widely in industrial processes especially electroplating industries for centuries in the form of soluble salts of Cr (VI) ions. It has an important role in a variety of industrial sectors including textile dyes, electroplating, metal alloying, animal hide tanning, prevention of water corrosion, ceramic glazes, refractory bricks, and lastly industries of pressure-treated lumber (Rowbotham, Levy and Shuker, 2000; Zayed and Terry, 2003). Cr (III) is often to be used in the manufacturing of leather, textile, and steel in industries; while Cr (VI) is widely utilised in the industrial application of electroplating, chemical manufacturing, printing and dyeing, tanning, and metallurgy, as well as the industrial manufacture of textile and leather (Ukhurebor et al., 2021). Ukhurebor et al. (2021) also claimed that chromium as the major element in electroplating provides metals corrosive resistance and also surface hardness for a specific requirement in industries. Moreover, other applications can be observed such as chromium being used in the pipes in the cooling system to prevent rusting; chromic acid as the electrolytic solution in the electroplating industry; chromium sulfate used for collagen strands in the tanning industry; chromium trioxide for wood preservation; lastly chromium-based paint for brightly colouring (Kerur et al., 2021).

2.2.1 Impacts of Chromium (VI) on the Environment

This section briefly discussed the negative impacts due to Cr (VI) particles on the environment. The chromium existing in Cr (VI), is highly soluble and movable in highly toxic form. As compared to Cr (III), it causes more damaging and destructive impacts to the environment including animals and human beings (Kerur et al., 2021). Throughout the years, chromium pollution in industrial activities and its impacts on the soil and groundwater had gained serious concerns from various researchers. According to Shanker and Venkateswarlu (2019), there are hundred thousand of workers who were estimated to be potentially exposed to high levels of Cr (VI) which could cause severe health issues such as lung cancer. International Agency for Research on Cancer (IARC) had classified Cr (VI) as one of the human carcinogens regarding the inhalation of the contaminants when getting exposure to it (Sun, Brocato and Costa, 2015).

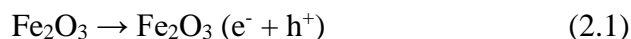
In the biological systems, the pollution of Cr (VI) leads to various types of harmful effects and accumulates within the environment involving living organisms. Humans had been encountered diseases and disorders due to the effects caused by Cr (VI) pollution even though in medium-low concentrations (Ukhurebor et al., 2021). According to Rajeswari (2014), heavy metals like chromium can be bonding to vital cellular components, causing their function to be inhibited. Long exposure to Cr (VI) can raise carcinogenic effects on the body, also endanger the health of human beings. Inhalation and retention of materials that contain Cr (VI) due to long-time exposure may lead to several health issues, including asthma, bronchitis, pneumonitis, liver inflammation, and bronchogenic carcinoma (Kotasâ and Stasicka, 2000). In addition, Cr (VI) element-containing chemical as contact with the skin body, can cause negative effects like allergies, dermatitis, necrosis and also corrosion of skin. In general, living organisms especially humans are exposed to Cr (VI) mainly in three paths, which are absorption through skin, ingestion, and inhalation of chromium-containing particles. The risk in terms of the health of an individual who is exposed to Cr-particles in a short distance for long hours, for example within an industrial site would be increased gradually (Ukhurebor et al., 2021).

2.2.2 Background of Chromium Removal Process: Iron Oxide as Cr (VI) Absorbent

Hexavalent chromium, Cr (VI) has been reported to be carcinogenic by nature which can cause severe health issues in humans, according to World Health Organization (WHO). Since 1947, a lot of techniques had been developed for Cr (VI) removal, including chemical precipitation, ion-exchange resin, coagulation, osmosis reversing, membrane filtration, and adsorption (Aigbe and Osibote, 2020). Among these removal methods for Cr (VI), metal oxide nanomaterials are commonly used for Cr (VI) absorption. Based on the research, iron oxide nanostructures have gained great interest due to its specific properties, including superparamagnetic nature, extremely small size (in nanoscale), high Curie temperature, and surface charge. Lockman (2018) stated that iron oxide α -Fe₂O₃ as the photocatalyst in the photocatalytic reduction is introduced to achieve redox transformation of Cr (VI) to Cr (III) since α -Fe₂O₃ is thermodynamically the most stable among the iron oxides series under ambient conditions.

The Cr (VI) reduction by iron oxide in aqueous solution is measured and discussed. As iron oxide α -Fe₂O₃ immersed in Cr (VI) solution is exposed to the light of 500 nm wavelength, the electron-hole pairs are produced within iron oxide, as shown in equation 2.1. The carries that are responsible for the process of redox transformation occurring on the iron oxide surface are holes for water oxidation as shown in equation 2.2, and electrons for Cr (VI) reduction as shown in equation 2.3 (Lockman, 2018). The reaction process is described as below:

Generation of carries:



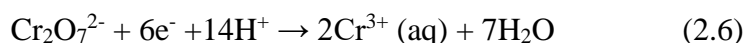
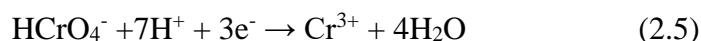
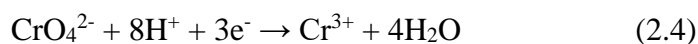
Water oxidation:



Cr (VI) reduction



The degradation of Cr (VI) on the surface of photocatalyst depends on the pH in an aqueous solution. The species of Cr (VI) like chromate (CrO_4^{2-}) and hydrogen chromate ion (HCrO_4^-) both are very mobile in which their reduction potentials (E^0) are greater than 1 V. Dichromate ($\text{Cr}_2\text{O}_7^{2-}$) ions are the dominating Cr (VI) species in a more acidic environment with greater reduction potentials. The reduction processes of CrO_4^{2-} , HCrO_4^- , and $\text{Cr}_2\text{O}_7^{2-}$ are shown in Equations 2.4, 2.5, and 2.6.



Lockman (2018) further stated that Cr (VI) reduction is a multi-proton reduction process, hence the reaction needs to be conducted in an acidic environment. Other than that, based on the reduction equations, the reduction should happen in the presence of sufficient potential electrons. However, photoreduction of Cr (VI) can be a slow process due to the slow kinetics of the oxidation in water. To ensure rapid Cr (VI) reduction, there are several parameters to be concerned, including the concentration of solute, nature of the solution, photocatalyst loading, light intensity, and temperature of the reduction process. The kinetic of Cr (VI) reduction process is affected by the complexity of the water to be remediated. Light intensity, as well as the light source may influence the kinetics of reduction as well. The increase in photon-flux can also increase the generation rate of electron-hole pairs, subsequently increasing the reduction rate. Moreover, in an open system, water can be evaporated due to the heat from the sun, altering the concentration of the solution of Cr (VI) ions and other unexpected thermally activated chemical reactions may occur (Lockman, 2018). In addition, catalyst loading can affect the kinetics of reduction in which higher loading may enhance and fasten the reduction of Cr (VI). In short, these parameters are the main factors to ensure rapid Cr (VI) reduction with iron oxide nanostructures.

2.3 Introduction of Iron Oxides

Iron oxides, the chemical compounds comprised of iron and oxygen, are widespread in the natural environment. They are present in the global system including the atmosphere, pedosphere, biosphere, and hydrosphere (Cornell and Schwertmann, 2003). Iron oxides have strong pigmenting power, where small quantities of elements can impart several vivid colours, including red, yellow, orange, reddish-brown, and blue-green. They are widely utilised in different applications such as pigments, catalysts, and absorbents for air and water purification. Besides, iron oxides can be used as components for animal feeding, automobile airbags, and magnetic tapes. Also, iron oxides are mostly the raw materials in the industries related to steel and iron (Suman et al., 2021).

According to Cornell and Schwertmann (2003), up to today, there are 16 types of iron-containing elements discovered including iron oxides, hydroxides, and oxide-hydroxides. Iron oxides family includes hematite (α - Fe_2O_3), magnetite (Fe_3O_4), wüstite (FeO), maghemite (γ - Fe_2O_3), β - Fe_2O_3 and ϵ - Fe_2O_3 . Iron generally exists in a divalent and trivalent state with its ions Fe^{2+} and Fe^{3+} . These oxides consist of closely packed oxygen arrays where octahedral and tetrahedral cavities are partially bonded with Fe^{2+} and Fe^{3+} ions (Suman et al., 2021). Fe^{2+} ion has an electron configuration of $1s^2 2s^2 2p^6 3s^2 3p^6 3d^6$; while Fe^{3+} ion is $1s^2 2s^2 2p^6 3s^2 3p^6 3d^5$. The outermost 3d electrons of iron determine the electronic and magnetic properties of different types of iron oxides formed.

2.3.1 Crystal Structures of Various Iron Oxides

2.3.1.1 Hematite (α - Fe_2O_3)

Hematite (α - Fe_2O_3) exists as the most stable iron oxide under atmospheric conditions. It is often utilised in gas sensors, pigments, also as the catalysts of different experiments since it has low cost and high corrosion resistance (Wu et al., 2015). Cornell and Schwertmann (2003) stated that hematite has a structure that consists of hexagonal closely packed (HCP) arrays of oxygen ions stacked in [001] direction. The plane of anions is parallel to the plane [001] as shown in Figure 2.1. Over half of the sites are bonded with Fe^{3+} ions that are arranged in a regular pattern with two filled sites, and one vacancy in

the [001] plane. This forms sixfold rings as in Figure 2.2. (Suman et al., 2021) stated that FeO_6 octahedra pairs are produced by the arrangement of cations. Each of the FeO_6 octahedron contributes its edges to 3 octahedra beside in the same plane while one of the faces is shared with the octahedron in an adjacent plane as shown in Figure 2.3 (Cornell and Schwertmann, 2003). The morphology of synthetic and geologic crystals of hematite can be found in plates, cubes, discs, rhombohedra, spheres, and ellipsoids (Suman et al., 2021).

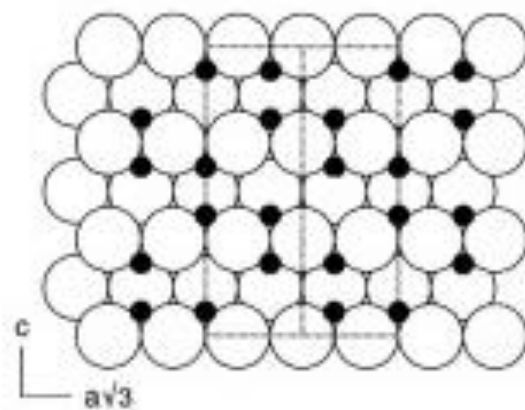


Figure 2.1: Oxygen in the HCP Structure with Cations Distributed in Octahedral Interstices (Cornell and Schwertmann, 2003).

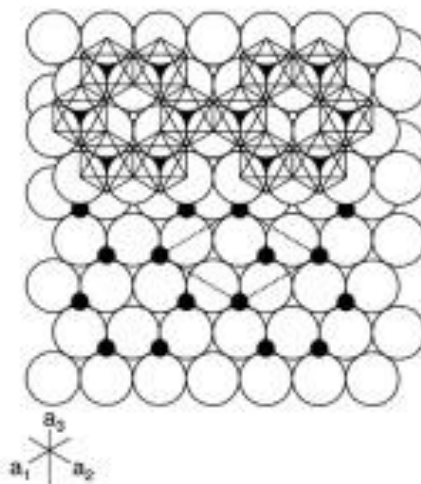


Figure 2.2: Distribution of Iron Ions Over Oxygen Layer and Octahedral Hexagonal Arrangement (Cornell and Schwertmann, 2003).

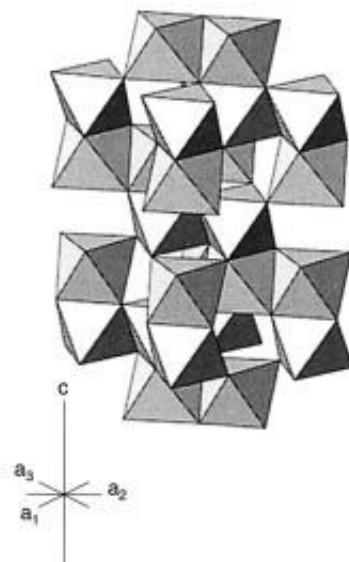


Figure 2.3: Octahedra Arrangement (Cornell and Schwertmann, 2003).

2.3.1.2 Magnetite (Fe_3O_4)

Cornell and Schwertmann (2003) proposed that magnetite has a face-centered cubic (FCC) unit cell which is consistently cubic close-packed along [111] arrangement based on 32 oxygen ions. The unit cell has an edge length of 0.839 nm and 8 formula units per unit cell. Magnetite is different as compared to other iron oxides as it consists of both divalent and trivalent valence states of iron ions. It has the inverse cubic spinel structure where Fe^{2+} ions fill up the octahedral sites for stronger crystal field stabilisation energy, meanwhile Fe^{3+} ions are equally occupying both tetrahedral and octahedral sites (Leonel, Mansur and Mansur, 2021). On the tetrahedral and octahedral sites, the structure of magnetite produces two magnetic sublattices of antiparallel spin moments, thus its ferromagnetic behaviour arises from the divalent cations magnetic moment (Ramimoghadam, Bagheri and Hamid, 2014; Hiemstra, 2018). Such inverse spinel structure provides superior magnetic properties, including high saturation magnetisation with $M_s \sim 92$ - 100 emu.g^{-1} and also magnetic susceptibility, making them be wisely used for biomedical application (Hedayatnasab, Abnisa and Daud, 2017; Ashraf et al., 2020). Figure 2.4 shows the structure of magnetite in (a) polyhedral model, (b) ball-stick model, (c) octahedral and tetrahedral ball-stick model.

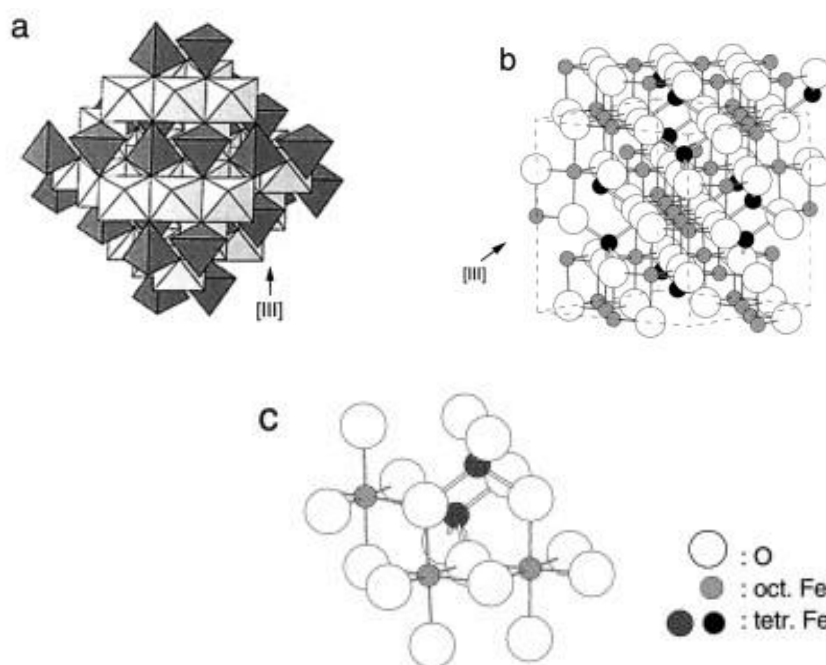


Figure 2.4: Structure of Magnetite (Fe₃O₄): (a) Polyhedral model, (b) Ball-stick Model, and (c) Octahedra and Tetrahedral Ball-stick Model (Cornell and Schwertmann, 2003).

2.3.1.3 Maghemite (γ -Fe₂O₃)

Maghemite (γ -Fe₂O₃) is having a similar structure as the oxide magnetite (Fe₃O₄) as one of the ferromagnetic oxides. Suman et al. (2021) also claimed that the chemical composition of maghemite is similar to the composition of hematite. Despite this, maghemite is known to be different compared to magnetite since most iron species exist in trivalent state. The cation vacancies compensate for Fe²⁺ ions oxidation by taking place within octahedral sites, thus maghemite is also known as the form of fully oxidised magnetite (Ashraf et al., 2020). According to Leonel et al. (2019), maghemite has a lower saturation magnetisation of $M_s \sim 80 \text{ emu.g}^{-1}$ but owning the advantages of being more stable and having higher resistance in acidic environments that is useful under some adverse conditions.

2.3.1.4 Wüstite (FeO)

Wüstite has the nominal formula of FeO. A stable, cation deficient phase of wüstite is written as Fe_{1-x}O, where the range of 1-x is fall between 0.83 and 0.95, which exists at 0.1 MPa pressure under high temperature (more than

567 °C) (Cornell and Schwertmann, 2003). Wüstite is said to be consisting of interpreting the face-centered-cubic structure of divalent iron (Fe^{2+}) and oxygen, (O^{2-}) ions. A cubic-close-packing structure array of anions are stacked along [111] direction, while the planes of cations are alternating with the planes of anions. Cornell and Schwertmann (2003) also stated that most of the iron has the interstices in octahedral with less trivalent iron (Fe^{3+}) on the vacant tetrahedral sites, while the Fe^{2+} ions and oxygen layers alternate along [111] as shown in Figure 2.5.

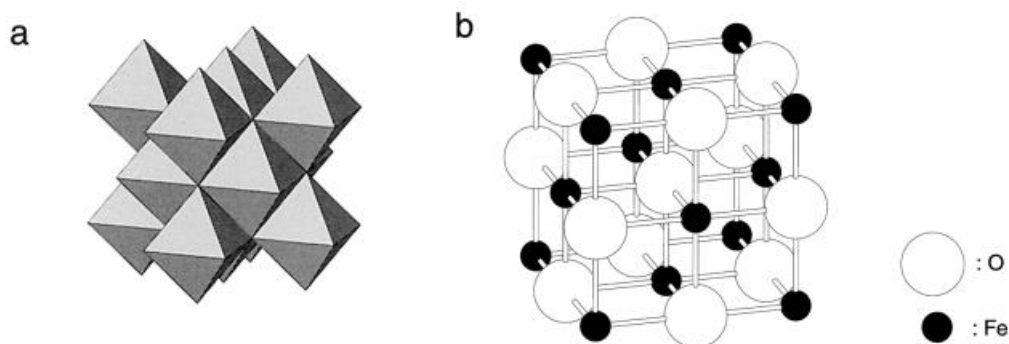


Figure 2.5: (a) Octahedral Arrangement of Wüstite and (b) Ball-stick Model of Wüstite (Cornell and Schwertmann, 2003).

2.3.2 Basic Properties of Iron Oxides

Due to the closely packed structure and high composition of iron elements, iron oxides are significantly having a higher density than most other minerals found in soils and sediments. Iron oxides are found that their densities are between 4.0 and $5.3 \text{ Mg}\cdot\text{m}^{-3}$ (Cornell and Schwertmann, 2003; Suman et al., 2021).

Iron oxides including hematite, magnetite, maghemite, and wüstite are known as semiconductors while among them magnetite performs almost metallic properties. According to Cornell and Schwertmann (2003), iron oxides as semiconductors, have the condition where the separation between their valence and conduction band of orbitals is lower than 5 eV . Electrical conductivity is mainly caused by free-charge carriers' motion in the solid, which is either the electrons in empty conduction band or the holes in full valence band. Intrinsic non-stoichiometry or the doped particles present in the structure results in moving of electrons. To allow the electrons to move over

the band gap into conduction band, a sufficient of energy that exceeds the band gap energy is necessarily required. With semiconductor properties, most iron oxide achieves electron excitation by irradiation with visible light of a suitable wavelength (Cornell and Schwertmann, 2003). In iron oxides, electrons can recombine with the vacancies and later being neutralised, thus decreasing the solid photo-activity. The degree of the recombination relies on the level of the pH of the solution and the effect on the iron oxide proportion at the surface.

2.4 Iron Oxide Nanostructures

2.4.1 One-Dimensional Iron Oxide Nanostructures

Over the past century, 1-D iron oxide nanostructures were widely studied and investigated due to their various uses in different fields including magnetic refrigeration, information storage, photocatalysts, pigment, and gas sensors (Chen et al., 2011). Iron oxide nanostructure materials own an important place in the nanotechnology field as they present a high surface-area-to-volume ratio, causing them to be extremely reactive, versatile, and strong compared to their counterpart (Hedayatnasab, Abnisa and Daud, 2017). According to Ashraf et al. (2020), characteristics of iron oxide nanostructure material including its controllable size, low toxicity, great magnetic properties, and high surface area allow them to be utilised for sustainable energy consuming and pollution control for environment.

In general, the nanomaterial is defined as a material with its external dimension in nanoscale, as well as internal or surface structure. Regarding the dimensions that are not constrained to the nanoscale range of less than 100 nm, nanomaterials can be categorised as zero-dimensional, one-dimensional, two-dimensional, or three-dimensional. The nanoscale is its length range approximately from 1 to 100 nanometers. 1-D nanomaterials have one of the dimensions that fall outside the nanoscale (1~100 nm). They can be microns or millimeters in length, but with a diameter of fewer than 100 nanometers (Lockman, 2018). The schematics of various forms of 1-D nanostructures including (a) nanorod, (b) nanowire, (c) nanoneedle, and (d) nanotube are shown in Figure 2.6. These schematics of 1-D nanostructures are based on

the morphologies of transition metal oxides synthesis through the thermal oxidation process.

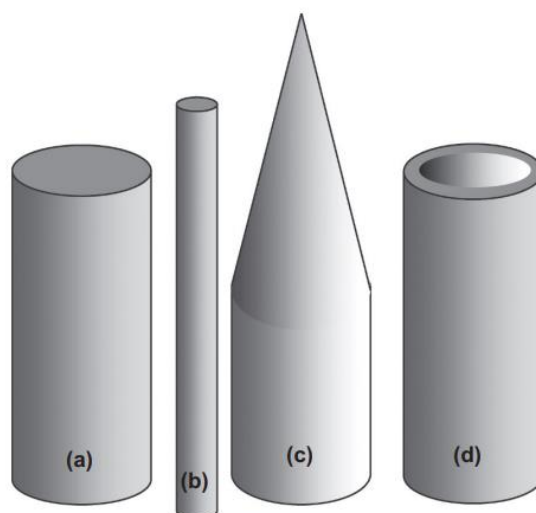


Figure 2.6: Schematics of 1-D Nanostructures: (a) Nanorod, (b) Nanowire, (c) Nanoneedle, and (d) Nanotube (Lockman, 2018).

Among the 1-D metal oxide nanostructures shown in Figure 2.6, nanowire and nanorod are the 1-D nanostructures with their diameters less than or equal to 100 nm. As compared to nanowires, nanorods are claimed to have a shorter length with a diameter larger than nanowires in certain cases (Ding and Wang, 2004). Meanwhile, nanoneedle refers to the 1-D nanostructure with a sharp tip. Lastly, the nanotube is not a common type of nanostructure that found on those metal oxides that undergoing thermal oxidation but, is commonly found in anodised metal oxides (Lockman, 2018).

2.4.2 Synthesis of Iron Oxide Nanowires

Iron oxide nanowires are commonly synthesised by thermal oxidation. A study on the iron oxide nanowires synthesis process via thermal oxidation was conducted by Budiman et al. (2016a) in the atmosphere of water vapour at different temperatures. As the iron is oxidised in the atmosphere of water vapour, the iron oxide nanowires formed is observed to be more obvious since the presence of water vapour enhances the oxidation rates of the iron as compared to the oxidation that occurs under dry atmosphere (Yuan et al., 2013). Pure iron foils with the dimension of 1 cm × 1 cm were prepared and

subjected to a grinding process using sandpaper to ensure the surface of iron foils is free from native oxide (Budiman et al., 2016b). The iron foil was cleaned, rinsed and later placed in a furnace for the oxidation process at 300, 400, and 500 °C in the atmosphere of dry air and water vapour. At high temperatures, iron is exposed to oxygen, forming a layer of oxide on the surface. Hematite ($\alpha\text{-Fe}_2\text{O}_3$) on the surface with the inner layer of magnetite (Fe_3O_4) is formed as if the oxidation temperature is kept under 570 °C (M. K. Chen and K. Olukotun, 2003; Yuan et al., 2012b). The sample is heated up at the rate of 5 °C/min for 2 hours, then is cooled in the furnace.

The morphologies of iron oxide nanostructures at different temperatures mentioned above, under the atmosphere of water vapour or dry oxygen are shown in Figure 2.7. The nanostructure of the iron oxide formed is observed using Field Emission Scanning Electron Microscope (FESEM). In Figure 2.7 (a), with the sample iron foil undergoing thermal oxidation at temperature of 300 °C, the oxide is observed to be rather flat with very small nanowires grown on its surface (Budiman et al., 2016a). As the heating temperature increased to 400 °C as shown in Figure 2.7 (b), it can be observed that the nanowires grown is denser, as the overall surface of the substrate is covered by the iron oxide nanostructure uniformly. Some of the iron oxide nanowires became slightly flat and flaky before transforming into nanosheets. Other than the thermal oxidation conducted under water vapour atmosphere, oxidation of iron foil was also carried out in dry air condition at 400 °C and 500 °C to observe the effect of water vapour on the nanostructure grown on the surface (Budiman et al., 2016a). In Figure 2.7 (d), when the iron foil was undergoing oxidation at 500 °C in water vapour, nanowires with more densely packed known as nanosheets were formed. Figure 2.7 (e) shows the nanowires on the iron foil grown by oxidation at 500 °C in condition of dry air. Meanwhile, for the iron foil sample that being oxidised at 400°C, it can be observed that there were more and longer nanowires produced in the environment with water vapour which is shown in Figure 2.7 (b) as compared to the sample oxidised in dry air condition, as shown in Figure 2.7 (c). The magnification images of nanowires can be observed as shown in Figure 2.8.

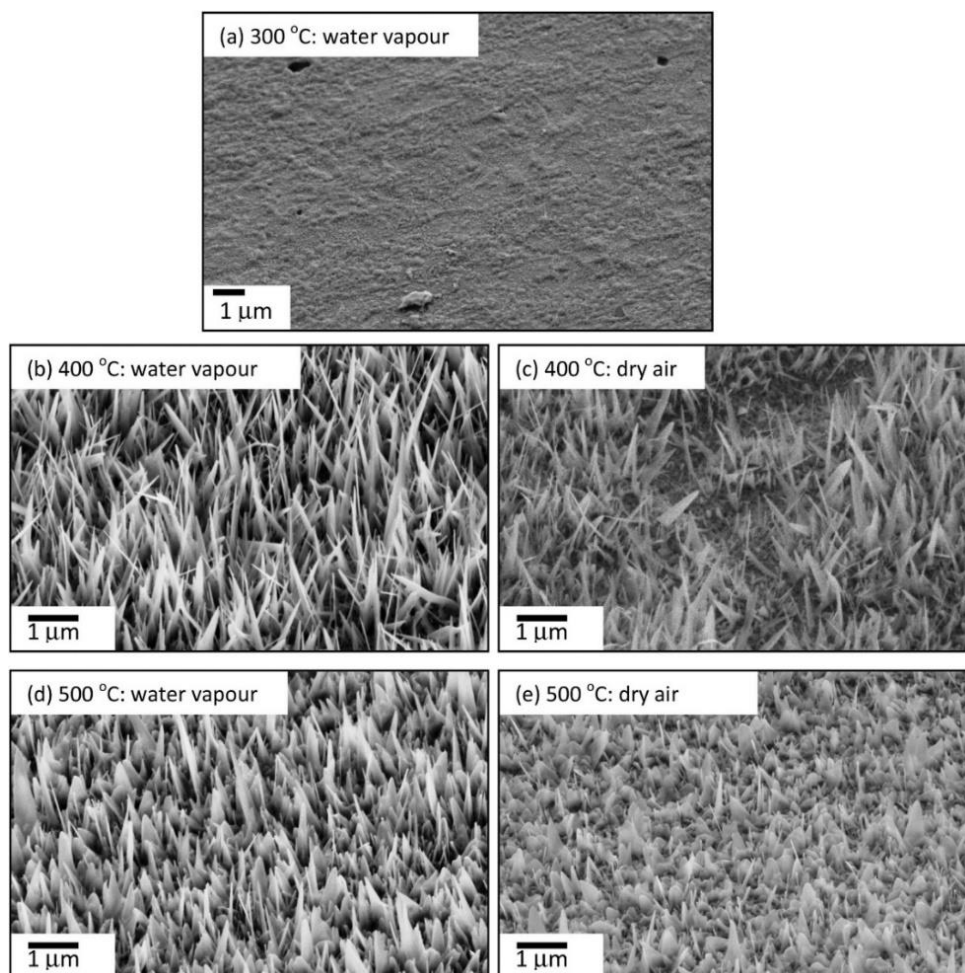


Figure 2.7: Images of Nanowires Obtained from FESEM: (a) 300 °C (Water Vapour), (b) 400 °C (Water Vapour), (c) 400 °C (Dry Air), (d) 500 °C (Water Vapour), and (e) 500 °C (Dry Air) (Budiman et al., 2016a).

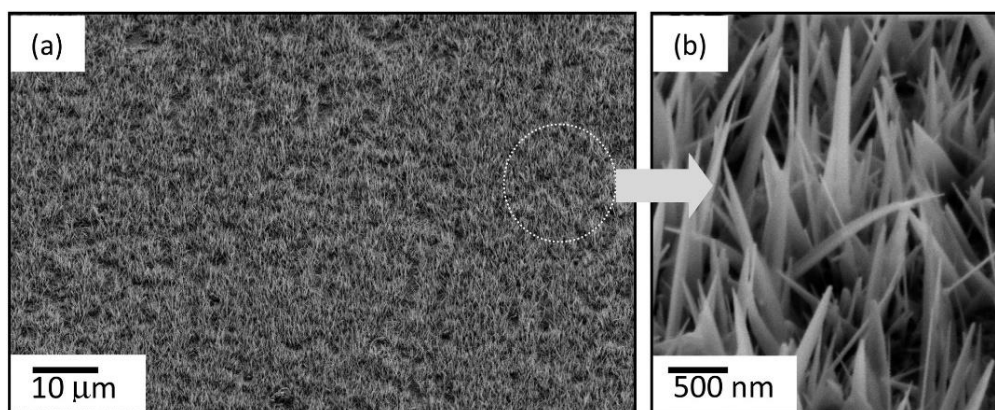


Figure 2.8: FESEM Magnification Images of Nanowires at 400°C in Water Vapour (Budiman et al., 2016a).

2.4.3 Growth Mechanism: Iron Oxide Nanostructures Grown by Thermal Oxidation

In general, metal oxide nanostructures have a growth mechanism using vapour-solid (VS) or vapour-liquid-solid (VLS). VS mechanism requires evaporation and corresponding condensation of precursor so that the structures can be formed, while VLS needs a specific catalyst for transpiration of uniaxial growth (Yuan et al., 2012a). However, this kind of mechanism is not followed in the iron oxide nanostructures formation via thermal oxidation since iron has a high melting point (Budiman et al., 2016b). The growth of iron oxide ($\alpha\text{-Fe}_2\text{O}_3$) is mainly driven by the relief of compressive stress at the interface between $\alpha\text{-Fe}_2\text{O}_3$ and Fe_3O_4 (magnetite) due to the solid-state transformation (Hiralal et al., 2008). The compressive stresses are formed due to the specific volume differences of the oxide layers. Researchers such as Hiralal et al. (2008) and Budiman et al. (2016a) proposed that from the iron foil sample (parent substrate), the iron atoms diffuse along a tunnel on the core of a screw dislocation of the nanowire, and then react with the oxygen atoms exist in the atmosphere where oxidation happens.

Despite this, Yuan et al. (2012b) has proposed a more detailed thesis in discussing the growth mechanism of hematite nanowires and nanobelts that are being synthesised in thermal oxidation. The growth mechanism of nanowires and nanobelts is shown in Figure 2.9. Based on the mechanism shown, the growth of the nanostructures is believed to be stimulated due to the interfacial reaction at the interface of $\alpha\text{-Fe}_2\text{O}_3$ and Fe_3O_4 . Normally, iron atoms move towards the surface of the substrate through grain boundary diffusion which requires lesser energy (Aquino et al., 2018). However, at greater and stronger interfacial reaction rates such as the increased oxygen partial pressures, the compressive stresses on the interface of $\alpha\text{-Fe}_2\text{O}_3$ and Fe_3O_4 will increase as well, thus also allowing the iron atoms to move through lattice diffusion instead of only through grain boundary diffusion. The growth of the nanostructures involves a combined diffusion mechanism of the iron atoms from the parent substrate onto the surface, as shown in Figure 2.9 (a) nanowire and (b) nanobelt (Hiralal et al., 2008; Yuan et al.,

2012a; 2012b). Later, the concentration gradient drives the growth of the nanostructures by diffusion happened on the surface of metal oxide.

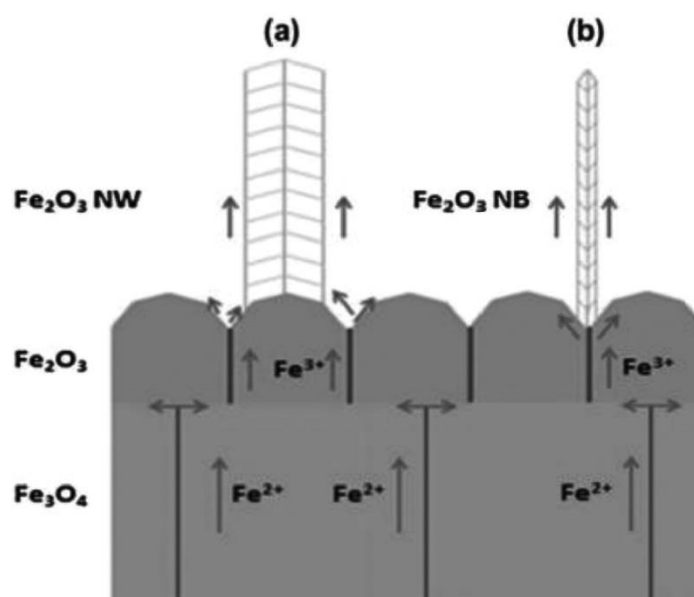


Figure 2.9: Mass Transport Mechanism of Iron Ions for Growth of Iron Oxide (a) Nanowire and (b) Nanobelt (Aquino et al., 2018).

2.5 Thermal Oxidation

Thermal oxidation method is one of the easiest processes to grow various metal oxide nanostructures, including nanowires or nanosheets, nanoneedles, and nanoflakes on the surface of bulk metals (Malwal and Packirisamy, 2018). This process has its advantages including rapid production of metal oxide nanostructures on a large scale yet convenient without involving hazardous materials (Zhao et al., 2013). Direct heating of metal substrates like foils, bars, plates, occurs at a temperature range from 400 °C to 800 °C in the presence of oxygen (Liu, Zhong and Tang, 2013), or a specific oxidising environment. There are several heating methods including heating in a furnace, resistive, flame, and plasma. In general, thermal oxidation requires a furnace as the heating system and metals as the reactants. Oxidation is commonly known as the transfer of electrons happening on metal to absorb oxygen molecules, forming oxygen ions O²⁻ (Lockman, 2018).

Thermal oxidation can be described as one type of corrosion but occurs in a dry state (Rahmat et al., 2020). In the oxidation of iron, native oxide is grown on its surface at ambient temperature, this process is also

known as rusting of iron, often leading to the degradation of iron. Despite, at an elevated temperature, the iron atoms have higher kinetic energy. The oxide film will continue to grow and thicken, causing an oxygen gradient across the oxide layer formed. This may affect and interfere the composition of the oxide scale based on different oxidation conditions. According to Schwertmann and Cornell (2000), the forming of oxide scale in the oxidation of iron is much more complex since it consists of discrete layers with various phases. At a temperature above 570 °C, the oxidation of iron forms an oxide scale which consists of various forms of iron oxides, including hematite (α - Fe_2O_3), magnetite (Fe_3O_4), and also wüstite (FeO). However, iron oxides only exist in the forms of hematite and magnetite at the oxidation temperature set below 570 °C. Figure 2.10 shows the SEM image of iron oxides that is oxidised at oxidation temperature of 500 °C, where the upper layer is the upper thin hematite layer is said to have wire or sheet structures while the magnetite layer formed below has a porous structure, according to the research done by Budiman et al. (2016a).

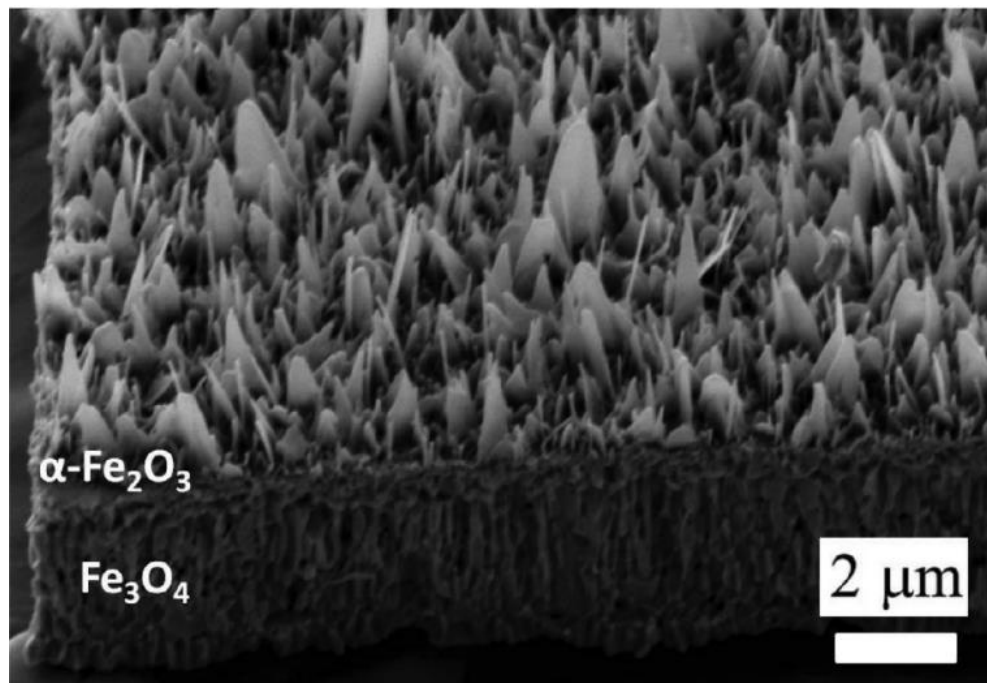


Figure 2.10: SEM Images of Iron Oxidised at 500 °C for 2 h (Budiman et al., 2016a).

2.5.1 Background of Thermal Oxidation for the Synthesis of α -Fe₂O₃ Nanowires

The first formal and comprehensive study on the synthesis of iron oxide α -Fe₂O₃ nanowires (also known as iron oxide “blades” or “whiskers”) by thermal oxidation was conducted by Takagi (1957) in Japan. In the study, several factors that would affect the condition of the iron oxide whiskers synthesised, such as oxidation environment, temperature, and the surface condition of the iron substrates were proposed by Takagi (1957). Based on the assessment conducted, the optimum oxidation condition for the iron oxide whisker structure to be synthesised was at the oxidation temperature within 400 - 850 °C, with the iron foil surface cleaned by electropolishing.

Upon entering the new era with the existence of nanotechnology, the term “whiskers” was no longer been used, the structure of the oxide was then named as nanowires instead. Some of the recent works reviewed are found to be focusing on the synthesis of iron oxide nanowires with high areal density and less oxidation time as possible. Fu et al. (2003) had successfully conducted an assessment on large arrays of aligned hematite nanowires synthesis through thermal oxidation of iron at the temperature of 600 °C for a duration of 10 hours under the specific atmosphere that consisted of carbon dioxide, silicon dioxide, nitrogen dioxide, and water. Besides, a study on the effect of the pressure of oxygen, temperature, and time of annealing during oxidation was conducted, where the results obtained proved that the increase in oxidation time and temperature will lead to the increase in the density and size of the nanowires (Hiralal et al., 2008). Moreover, Srivastava et al. (2011) had done an investigation on the effects of iron texture on the synthesis of iron oxide nanowires, reported that iron oxide nanowires were found to be grown on the grain orientation of [110], while the dimension including length and width of nanowires might vary due to the oxidation condition.

According to the literature review studied, the largest width of iron oxide nanowires could be found as large as 150 nm, meanwhile, the length was found to be varied ranging from 0.1 to 5 microns. Table 2.1 summarises several famous works conducted by different researchers as a literature review on the thermal oxidation process for iron oxide (α -Fe₂O₃) nanostructures synthesis over the past decade.

Table 2.1: Summarised Literature Review on Iron Oxide Nanostructures Synthesised via Thermal Oxidation.

Morphology	Thermal Oxidation Condition			Researchers
	Temperature (°C)	Time	Oxidation Atmosphere	
α -Fe ₂ O ₃ whiskers	400 - 850	-	Air	Takagi (1957)
α -Fe ₂ O ₃ micron-size blades	600	1 h	O ₂	Voss, Butler and Mitchell (1982)
α -Fe ₂ O ₃ nanowires	550 - 650	10 - 30 h	CO ₂ , N ₂ , SO ₂ , and H ₂ O vapour	Fu et al. (2003)
α -Fe ₂ O ₃ bicrystalline nanowires	550 - 600	Few days	CO ₂ , N ₂ , SO ₂ , and H ₂ O vapour	Wang et al. (2005)
α -Fe ₂ O ₃ nanowires	800	10 h	N ₂ , O ₂	Wen et al. (2005)
α -Fe ₂ O ₃ nanowires	550 - 650	10 - 120 h	CO ₂ , N ₂ , SO ₂ , and H ₂ O vapour	Han et al. (2006)
α -Fe ₂ O ₃ nanowires	700	2 - 4 h	Ozone-rich environment	Srivastava et al. (2007)
α -Fe ₂ O ₃ nanowires	400 - 620	1 - 10 h	Ar and O ₂	Hiralal et al. (2008)

α -Fe ₂ O ₃ nanowires	350	10 h	Air	Hsu et al. (2008)
α -Fe ₂ O ₃ nanowires	255	24 h	Air	Hiralal et al. (2011)
α -Fe ₂ O ₃ nanowires	700	16 h	Moist O ₂	Srivastava et al. (2011)
Quasi 1-D α -Fe ₂ O ₃	280 - 480	-	Air	Zhong et al. (2011)
α -Fe ₂ O ₃ nanowires	400, 600	1 h	Low concentration O ₂	Yuan et al. (2012b)
α -Fe ₂ O ₃ nanorods and nanocorals	600 - 800	8 – 10 h	O ₂ and Ar gases	Vincent et al. (2011)
α -Fe ₂ O ₃ platelet, corals, and nanowires	600	1 h	Air	Grigorescu et al. (2012)
α -Fe ₂ O ₃ nanorods and nanosheets	500, 800	2 h	Water vapor	Budiman et al. (2016b)
α -Fe ₂ O ₃ nanorods and nanosheets	300 - 500	2 h	Dry air/water vapour	Budiman et al. (2016a)

2.5.2 Effect of Thermal Oxidation Parameters on the Iron Oxide Nanostructures

The synthesis of iron oxide nanostructures is the function of various operating parameters, including oxidation temperature, time and also the atmosphere during the experiment. In this subsection, the effects of the parameters mentioned are studied through the assessments done by previous researchers (Lockman, 2018).

2.5.2.1 Effect of Oxidation Temperature and Growth Time

Thermal oxidation of iron occurs spontaneously in the ambient environment, but the oxide layer that formed under ambient conditions does not exhibit the morphology of nanostructures (Hiralal et al., 2008). Different iron oxide layers can be formed on the iron substrate according to specific oxidation temperatures. Budiman et al. (2016b) proposed that a multilayer of Fe_3O_4 and $\alpha\text{-Fe}_2\text{O}_3$ oxide film is formed on the metal substrate at oxidation temperatures below $570\text{ }^\circ\text{C}$; whereas a multilayer consists of Fe, FeO, Fe_3O_4 , and $\alpha\text{-Fe}_2\text{O}_3$ is grown at higher oxidation temperature than $570\text{ }^\circ\text{C}$. The cross-sectional iron oxide nanostructures synthesised at the oxidation temperature of $400\text{ }^\circ\text{C}$ and $600\text{ }^\circ\text{C}$ are shown in Figure 2.11.

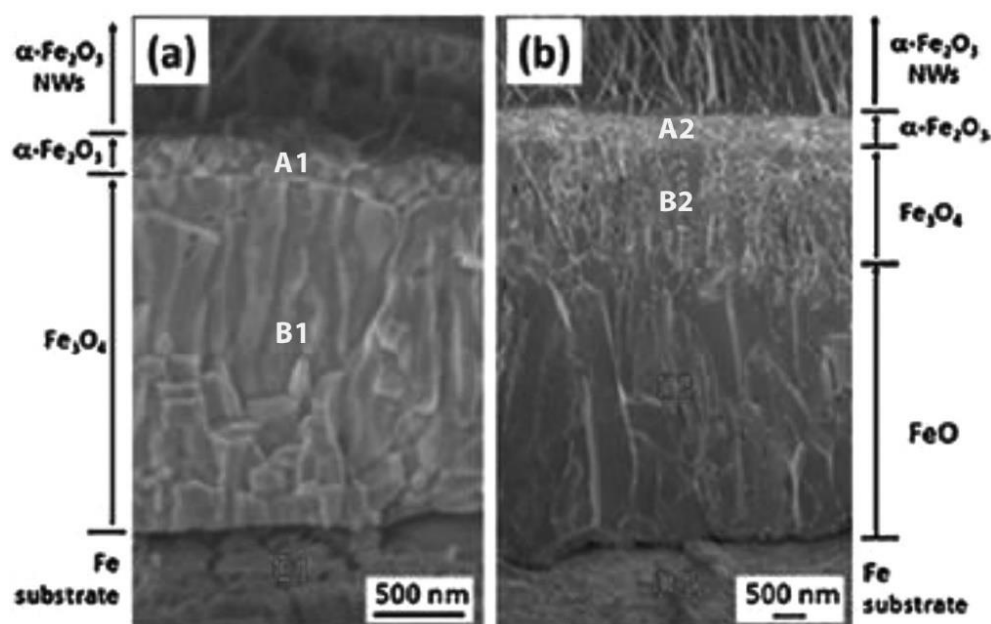


Figure 2.11: Cross Section of Iron Oxide Nanostructures at (a) $400\text{ }^\circ\text{C}$ and (b) $600\text{ }^\circ\text{C}$ of Oxidation Temperature (Yuan et al., 2012a).

According to the study proposed by Yuan et al. (2012a), FeO at oxidation temperature below 570 °C is thermodynamically unstable, thus it is observed that there is no FeO formed at the oxidation temperature of 400 °C as shown in Figure 2.11 (a). The grains of FeO and Fe₃O₄ are coarse and columnar in visual. However, the grains of α -Fe₂O₃ that contact directly with the nanowires, consist of finer grains as compared to previous oxides mentioned. In Figure 2.11 (a), the Fe₃O₄ layers have a thickness of around 2 μ m while α -Fe₂O₃ layers have approximately 250 nm of thickness. On the other hand, a three-layered structure consists of FeO, Fe₃O₄, and α -Fe₂O₃ is shown in Figure 2.11 (b), each with a thickness of 5, 2, and 0.4 μ m, respectively (Yuan et al., 2012a; 2012b). With the results obtained, it can be deduced that the FeO layer is not essential to the synthesis of iron oxide nanowires. The oxides α -Fe₂O₃ are always grown at the top surface with a significant nanowire morphology. As going deeper into the layers of oxide, the oxidation of iron becomes weaker due to increasing difficulty for the transport of reacting species, thus there are only lower oxides like FeO formed within the region. Hiralal et al. (2008) stated that α -Fe₂O₃ can be directly tuned into nanostructure form in the thermal oxidation process since lower oxides often exist as sublayers under the hematite layer.

In a reducing atmosphere, the post-treatment of the iron oxide α -Fe₂O₃ formed would alter the stable phases, as shown in the X-ray diffraction (XRD) pattern of iron oxide nanowires synthesised at various temperatures in Figure 2.12 (Grigorescu et al., 2012). The sharp peaks in the XRD pattern refer to the high degree of crystallinity of both oxides α -Fe₂O₃ and Fe₃O₄. The increase in intensities due to the increasing temperature proved that more hematite phases can be formed and a slight increase in the thickness of oxides is observed at a higher temperature.

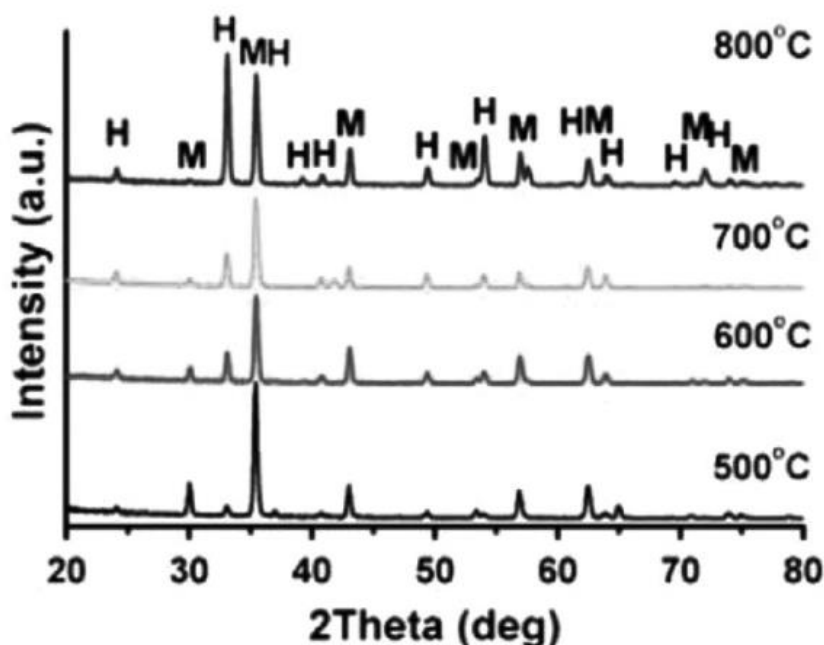


Figure 2.12: XRD Patterns of Iron Oxide Sheets Formed at Different Temperatures (Grigorescu et al., 2012).

Referring to the results generated, it can be deduced that the density of iron oxide nanowires increases as the oxidation temperature increases, as well as the oxidation rates. The diameter, length, and growth rate can be seen to increase with temperature (Hiralal et al., 2008). With the oxidation rates increased, smaller $\alpha\text{-Fe}_2\text{O}_3$ grain size can be synthesised and thus, providing more diffusion paths for the transport of atoms. Wider nanowires are observed at higher oxidising temperatures (Budiman et al., 2016a). Other than oxidation temperature, it is observed that the length of growth time for iron oxide nanowires also affects the morphology of nanostructures formed. Hiralal et al. (2008) proposed that the oxidation of iron occurs at the early stages, later the growth proceeded with time. Due to the oxidation mechanisms mentioned in Section 2.4.2, a longer growth time helps in the uniaxial growth of the iron oxide nanostructures, resulting in the formation of longer needle-like structures for the oxidation of iron. In short, the effects of oxidation temperature and time for the growth of iron oxide nanostructures are determined.

2.5.2.2 Effect of Oxidation Atmosphere

By varying the atmosphere or environment of thermal oxidation, the surface morphology of iron oxide nanostructures can be tuned. According to the investigation done by Hiralal et al. (2008; 2011), the morphology of the iron oxide nanostructures on the surface and their size were not affected by different partial pressure of oxygen as thermal oxidation was conducted. Nevertheless, the oxide layers formed were found to have an increase in thickness at higher oxygen partial pressure. Also, the diameter of the iron oxide nanowires synthesised was observed to decrease under this condition but no obvious change in the height of the nanowires. The decrease in nanowires diameter led to a greater density of nanowires formed in thermal oxidation (Yuan et al., 2012a; 2012b).

The thermal oxidation for iron oxide nanostructures synthesis in water vapour had been investigated in Section 2.4. Water vapour present in the oxidation environment greatly affected the surface morphology and the density of the iron oxide hematite phase in a shorter time (Budiman et al., 2016b). From the results obtained in the experiment, oxidation of iron for 60 min at 500 °C in water vapour produced denser mixture of nanowire and nanosheet (Budiman et al., 2016b). The structures of the iron oxide formed appear broader at the bottom part of nanowires and nanosheets. Budiman et al. (2016a; 2016b) further stated that as the oxidation time increased, an obvious lateral growth was observed where the tapered nanowires evolved into a blade-like appearance. In contrast, a needle-like morphology of iron oxide nanowires is observed in the oxidation in a dry air atmosphere. Therefore, the presence of water vapour would enhance the oxidation rates and promote the growth of iron oxide nanostructure in thermal oxidation. However, the enhancement in the growth rates of nanostructures would transform the structures of nanowires into nanosheets. Hence, oxidation in dry air is generally more desired in the formation of 1-D iron oxide hematite nanostructures as compared to oxidation in water vapour.

2.5.3 Thermal Oxidation with Potassium Halides

In general, process of thermal oxidation for metal oxide nanostructures synthesis are conducted under the atmosphere of dry air or water vapour.

However, it is possible to heat the transition metal at a specific temperature with the potassium halides such as potassium iodide (KI) or potassium bromide (KBr). Research on the preparation of tungsten oxide nanowires via thermal oxidation with potassium halides was conducted by Qi, Wang and Liu (2003). In this assessment, highly oriented potassium-doped tungsten oxide nanowires were produced by heating the tungsten metal with potassium halides in air. The process was carried out in the furnace similar to the thermal oxidation of other transition metals, but the metal tungsten was covered by potassium halide powder. The sample was heated in air for 2 hours at the oxidation temperature of 625 – 650 °C and rinsed with deionised water after being cooled down slowly to ambient temperature.

Based on the result obtained, it was observed that the presence of potassium halides is important for the formation of tungsten oxide nanowires at higher oxygen concentrations. To prove that, a sample of tungsten metal was treated under similar conditions without being covered with potassium halide powder. However, the nanowires were not synthesised at the condition. Figure 2.13 shows the flower-like nanowires formed on the tungsten metal plate that are deposited with potassium halide grains. It is observed that the nanowires were grown on the area that was deposited with potassium halide. The result indicates that the tungsten oxide nanowires have a formation mechanism that involves the reaction between potassium halide (salt), tungsten, and oxygen (Qi, Wang and Liu, 2003). The nanowires produced only consist of potassium, tungsten, and oxygen.

From the oxidation of tungsten and potassium iodide, low melting point tiny droplets containing potassium, tungsten, and oxygen were produced. These droplets are the seeds or templates for the growth of nanowires (Qi, Wang and Liu, 2003). Solid $K_2W_4O_{13}$ precipitated from the droplets in the nanowire form as more tungsten oxide was dissolved to reach the supersaturating state. The growth of nanowires was sustained by continuous feeding of WO_3 and K_2O . The size of the nanowires formed in this experiment is affected by the size of the liquid droplet produced as mentioned above. Hence, it is crucial to control the conditions carefully so that large liquid droplets would not be formed. However, Qi, Wang and Liu (2003) also proposed that nanowires would not be able to form if the

oxidation temperature is set higher than the melting point of potassium halide involved in the experiment. This is because at that condition the potassium salt on the surface of the tungsten plate will completely melt into liquid, thus no tiny droplets can be formed for the synthesis of nanowires.

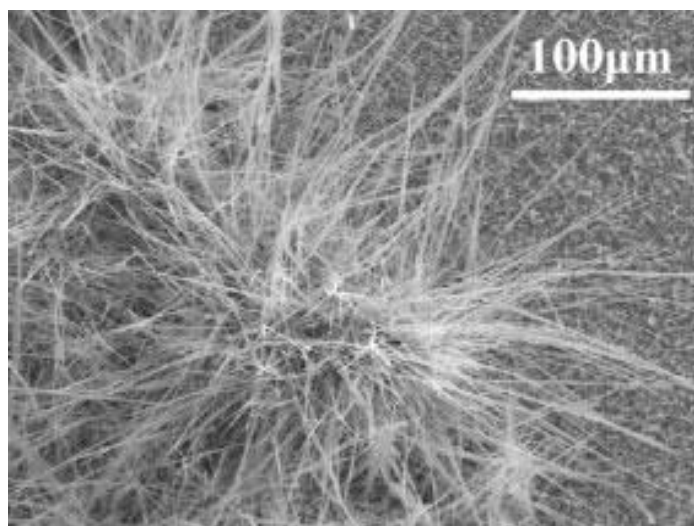


Figure 2.13: Nanowires Formed at the Part Deposited with Potassium Halide Grains (Qi, Wang and Liu, 2003).

2.6 Summary of Literature Review

In short, the issues regarding the Cr (VI) pollution need to be handled and treated seriously to prevent destructive effects on marine environment. The existence of Cr (VI) in water sources endangers the living organisms and easily causes death. Chromium absorption method was often proposed by various researchers due to its effectiveness and simplicity of the process. Iron oxide nanostructures are selected as the Cr absorbent material as it has superparamagnetic nature to absorb Cr (VI) ions from the polluted water. The iron oxide nanostructures can be synthesised by thermal oxidation in an easy and fast process. Various studies had been conducted to investigate the thermal oxidation process for iron oxide nanostructures growth. It is determined that several parameters such as oxidation temperature and time could affect the surface morphologies and phases of nanostructures grown. On top of that, potassium iodide is found to be useful in enhancing the formation of metal oxide nanostructures using thermal oxidation. Hence, it is

expected to improve the growth of iron oxide nanostructures via thermal oxidation.

CHAPTER 3

METHODOLOGY AND WORK PLAN

3.1 Introduction

This chapter mainly consists of three sections, including the material preparation for iron oxide synthesis, thermal oxidation process, and lastly the experimental test for the sample product synthesised under different experimental parameters. The preparation of the materials required in the experiments was discussed in the first section of this chapter. Next, the thermal oxidation process for the growth of iron oxide was described in the following section. In the thermal oxidation process, the heating temperature was manipulated for a specific range to observe the difference in results generated, as well as the heating time and oxidation atmosphere with the presence of potassium iodide. The last section in this chapter revealed the characterisation tests conducted to examine the sample product, iron oxide synthesised in the experiment. Three types of tests were conducted including scanning electron microscopy (SEM), X-ray diffraction (XRD), and chromium removal test.

3.2 Material for Experiments

In this research, iron foil was used as the substrate for the growth of iron oxide. Besides, potassium iodide powder was prepared and the sample iron foil was covered with the powder during thermal oxidation. Potassium iodide was expected to be able to speed up the time needed for iron oxide synthesis and enhance the growth of nanostructures on the sample foil (Qi, Wang and Liu, 2003). For the cleaning materials, the silicon carbide SiC paper grit 2000 was used to grind the surface of the iron foil, and the iron foil was ultrasonically cleaned with acetone and ethanol before initiating the oxidation process. The list of materials with descriptions is shown in Table 3.1.

Table 3.1: List of Experimental Materials.

Materials	Description
Iron foil	The substrate for the iron oxide nanowires to grow.
Potassium iodide powder	A catalyst to fasten the oxidation time and enhance the growth of iron oxide nanowires.
SiC paper grit 2000	To clean and grind the iron foil.
Acetone and ethanol	Cleaning reagent.

3.3 Thermal Oxidation Process

In this work, thermal oxidation was conducted to synthesise the iron oxide nanostructures. The iron foil with the thickness of 0.1 mm was cut into 1 cm \times 4 cm and the surface of the sample was cleaned through grinding using SiC paper grit 2000. Then each sample was ultrasonically cleaned in acetone and ethanol for 3 min each before undergoing thermal oxidation to ensure clean and free from dust and impurities. The iron foil was then rinsed with distilled water and dried with compressed air.

After cleaning the iron foil, it was placed on a crucible and positioned inside the muffle furnace to undergo thermal oxidation process. The iron foil sample was covered with 1 g of potassium iodide powder to observe its effects on the growth of iron oxide nanostructures. Figure 3.1 shows the muffle furnace used for thermal oxidation. To determine the effect of oxidation temperature on the nanostructures grown on the substrate, the thermal oxidation of the iron foil substrate was conducted under the temperature of 200, 300, 400, and 500 °C, respectively for 2 h with 5 °C/min of heating rate.



Figure 3.1: Muffle Furnace.

The sample with the best quality of nanostructures synthesised was then collected and the respective temperature was recorded. Then, a sample of iron foil was oxidised at the temperature recorded for different periods, including 0.5, 1, 1.5, 2, 2.5, and 3 h to determine the effects of oxidation duration on the iron oxide.

3.4 Experimental Characterisation Tests

When the synthesis process of iron oxide nanostructures sample was completed through thermal oxidation, several tests were conducted to investigate the morphology and structural properties of the various specimens produced. To study the morphology of the sample synthesised, SEM analysis was performed. Besides, the structural properties and phase identification of the samples produced were investigated by the X-ray diffraction (XRD) method. Last but not least, chromium removal test was conducted on the specimens synthesised to examine the removal efficiency of each specimen.

3.4.1 Morphological Analysis

The surface and the cross section morphology of the synthesised iron oxide nanostructures was examined using the equipment of SEM. The specimen was cut into the size of approximately $0.5 \text{ cm} \times 0.5 \text{ cm}$ and placed under the SEM microscope. The surface morphology and the dimensions of the nanostructures formed on the substrate were examined and calculated using high precision measuring software, ImageJ. Figure 3.2 shows the equipment

for scanning electron microscopy (Hitachi S-3400N) used to examined the surface morphology of the specimens.



Figure 3.2: Scanning Electron Microscope (Hitachi S-3400N).

3.4.2 Structural Analysis

The specimens produced by thermal oxidation process were examined by XRD analysis using X-ray diffractometer. The crystal structure and the phases of iron oxide nanostructures were studied and analysed. The samples were cut into the size of approximately $1\text{ cm} \times 1\text{ cm}$ for XRD analysis. The XRD analysis was conducted in the range $2\theta = 20\text{-}80^\circ$ under the settings of Cu $K\alpha$ radiation with the wavelengths, $\lambda = 0.154\text{ nm}$. The operating current and voltage were adjusted at 30 mA and 40 kV, respectively with the scanning rate of $2^\circ/\text{min}$. Figure 3.3 shows the X-ray diffractometer.



Figure 3.3: X-ray Diffractometer.

3.4.3 Chromium (VI) Removal Test and Analysis

3.4.3.1 Preparation of Chromium (VI) Solution

To conduct the chromium (VI) removal test on the specimens, the Cr (VI) stock solution was prepared. The concentration of the solution prepared was 10 ppm (parts per million), equivalent to 10 mg/L. Potassium dichromate, $K_2Cr_2O_7$ was dissolved with distilled water to achieve the solution with concentration of 10 mg/L. As 1 L of Cr (VI) solution required 10 mg of chromium, the weight ratio of Cr in $K_2Cr_2O_7$ was calculated to obtain the amount of $K_2Cr_2O_7$ needed for the Cr (VI) removal test. According to the calculation done, 28.29 mg (0.02829 g) of $K_2Cr_2O_7$ was required. However, low weight as 0.02829 g was difficult to be weighed. Hence, a method of dilution was proposed to obtain the required Cr (VI) solution. Cr (VI) solution was first prepared at a higher concentration of 100 mg/L. 1 L of 100 mg/L of Cr (VI) solution was prepared by using 0.2829 g of $K_2Cr_2O_7$ (scaling up to 10 times). Then, 100 ml of this solution was poured out and diluted with distilled water. With diluting, 1 L of Cr (VI) solution with the concentration of 10 mg/L was successfully prepared. The preparation of Cr (VI) solution is shown in Figure 3.4.



Figure 3.4: 100 mg/L (left) and 10 mg/L (right) of Cr (VI) Solution Prepared in Volumetric Flasks.

After the preparation of 10 mg/L Cr (VI) solution, 100 ml of Cr (VI) solution with 10 mg/L concentration was poured into a conical flask. There was approximately 35 μ L of concentrated sulphuric acid (H_2SO_4) added into the conical flask to obtain pH value of 2 in the Cr (VI) solution for the absorption test of the specimen. A pH indicator paper was used to determine the pH value of the solution as shown in Figure 3.5.

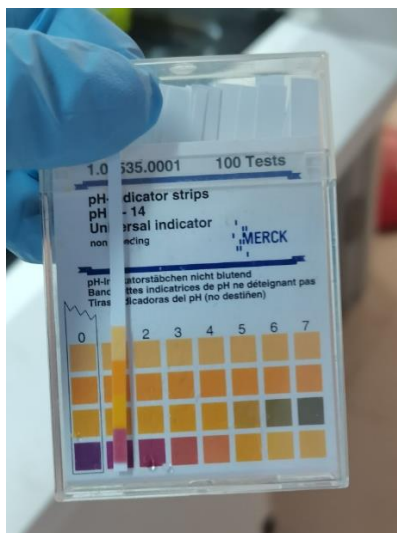


Figure 3.5: pH Indicator Paper Used to Identify the Acidity of the Solution.

3.4.3.2 Chromium Removal Test of Specimens

Prior to the Cr (VI) removal test, 2.5 ml of aliquot solution was firstly obtained from the 100 ml of 10 mg/L Cr (VI) solution by using a micropipette. Then, it was placed into a centrifugal tube. Next, the specimen synthesised from thermal oxidation with 1 cm \times 1 cm size was put into the conical flask containing the prepared Cr (VI) solution. An incubator shaker was used to shake the conical flask at the rotating speed of 150 rpm for 30 min as shown in Figure 3.5. Every 5 min, 2.5 ml of the aliquot solution was collected. This test was conducted to identify the removal efficiency of Cr (VI) ions by various specimens formed under synthesis parameters. A bare iron foil was also placed in the solution as a base reference.



Figure 3.6: Conical Flasks Shaken in the Incubator Shaker.

When the removal test was completed, a method named diphenyl-carbazide colourimetric method was used to analyse the efficiency of chromium removal on each sample produced. The 1,5-diphenyl-carbazide solution was produced by dissolving 0.05 g of diphenyl-carbazide powder in 10 ml of acetone. Also, 35 μL of 1,5-diphenyl-carbazide solution was added into every sample of aliquot solution. The amount of diphenyl-carbazide solution was determined by trial and error method to prevent the aliquot solution samples from becoming saturated condition during the ultraviolet-visible test. The samples were hand shaken vigorously to ensure a perfect mixing of the solution. In this test, the colourisation of the sample solution decreased as if the Cr (VI) concentrations in the solution were reduced. Figure 3.6 shows the aliquot solution sample mixed with 35 μL of 1,5-diphenyl-carbazide solution in the centrifugal tube.

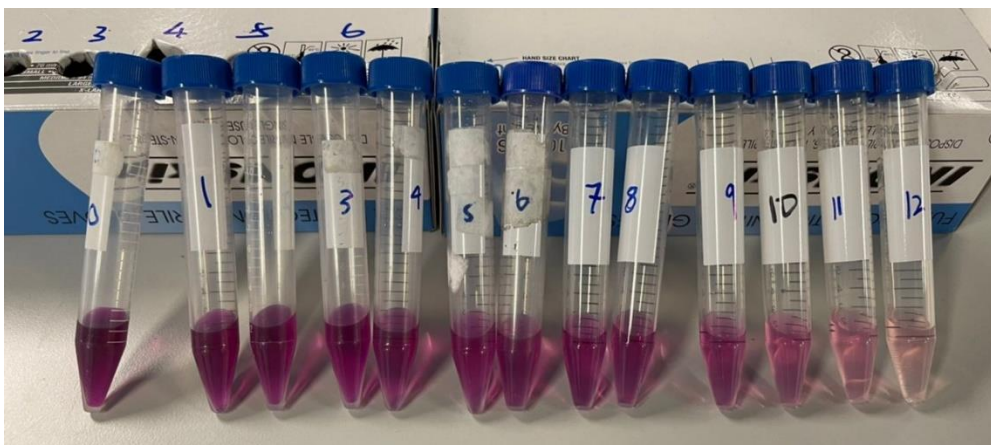


Figure 3.7: Aliquot Solution Sample Mixed with 35 μL of 1,5-diphenyl-carbazide Solution in the Centrifugal Tube.

Lastly, the sample solutions were transferred into the plastic cuvettes for ultraviolet-visible test as shown in Figure 3.8. Distilled water was selected as the blank reference for spectroscopy. These samples were scanned by the ultraviolet-visible spectrophotometer (Cary 100 Bio) as shown in Figure 3.8 at a wavelength ranging from 440 to 640 nm. The Cr (VI) removal efficiency was determined by referring to the absorbance level at the wavelength of 540 nm.

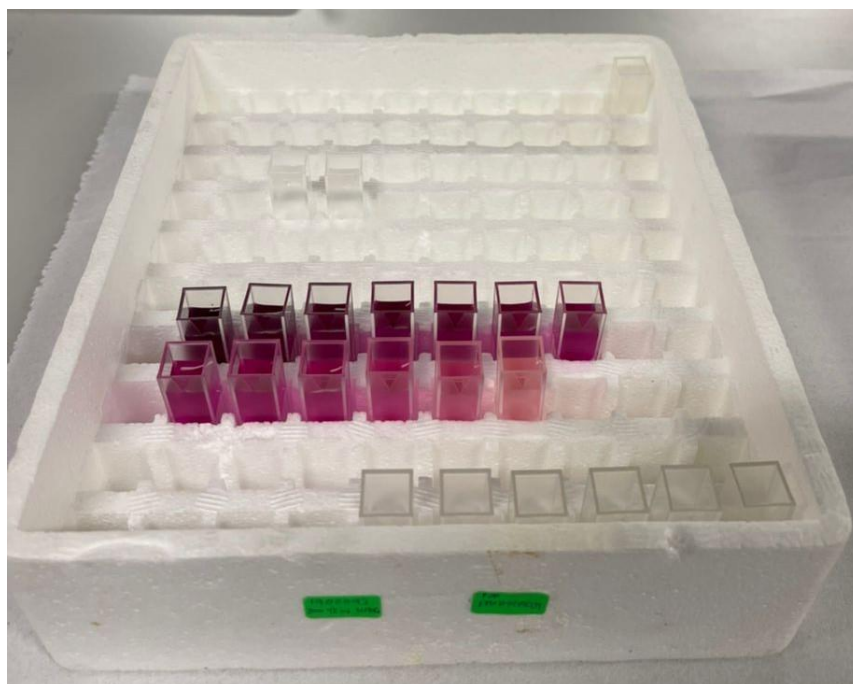


Figure 3.8: Aliquot Sample with Spectroscopy Blank in Plastic Cuvette for Ultraviolet-visible Spectrophotometry Analysis.



Figure 3.9: UV-VIS Spectrophotometer.

3.5 Summary

In this work, iron oxide nanosheets were synthesised through the thermal oxidation process. The optimum oxidation temperature and period in the presence of potassium iodide for iron oxide nanostructures growth were identified by comparing the quality of each specimen fabricated in terms of morphology, structural properties, and the Cr (VI) removal efficiency. The samples were studied and analysed using several methods, including SEM analysis to study the surface morphology of the specimens, XRD analysis to investigate the structural properties, and lastly the chromium removal test to identify the removal efficiency of each sample.

CHAPTER 4

RESULTS AND DISCUSSION

4.1 Introduction

In this chapter, the experimental results of the synthesised specimens obtained from the characterisation tests of scanning electron microscopy (SEM), X-ray diffraction (XRD), and chromium (VI) removal test were analysed and discussed. SEM was conducted to study the surface morphology of the iron oxides grown by thermal oxidation. Next, XRD was performed on the samples oxidised at 500 °C for different oxidation duration to examine and identify the phases existing on the iron oxide layer. Besides, Cr (VI) removal tests were also conducted to determine the efficiency of the sample produced in removing Cr (VI) ions.

4.2 Morphological Analysis: Scanning Electron Microscopy (SEM)

SEM was conducted on the iron oxide samples synthesised by thermal oxidation to examine the surface morphology of multiple samples formed under different oxidation parameters. The surface nanostructures of the specimens were observed using the scanning electron microscope under the magnification of 20 k. The dimensions of nanostructures produced on the surface of specimens were examined and calculated by a high precision measuring software, ImageJ. The effect of oxidation temperature, duration, and the presence of potassium iodide in thermal oxidation of iron foil were analysed and discussed in this section.

4.2.1 The Effect of Oxidation Temperature on the Growth of Iron Oxides

Thermal oxidation of the iron foils in the presence of potassium iodide at different temperatures including 200, 300, 400, and 500 °C were conducted to observe and analyse the growth of iron oxide nanostructures. The duration for the oxidation process was constantly set to 2 h to identify the effect of oxidation temperature on the specimens. The surface morphologies of the

oxidised specimens at different temperatures were examined by SEM analysis as shown in Figure 4.1.

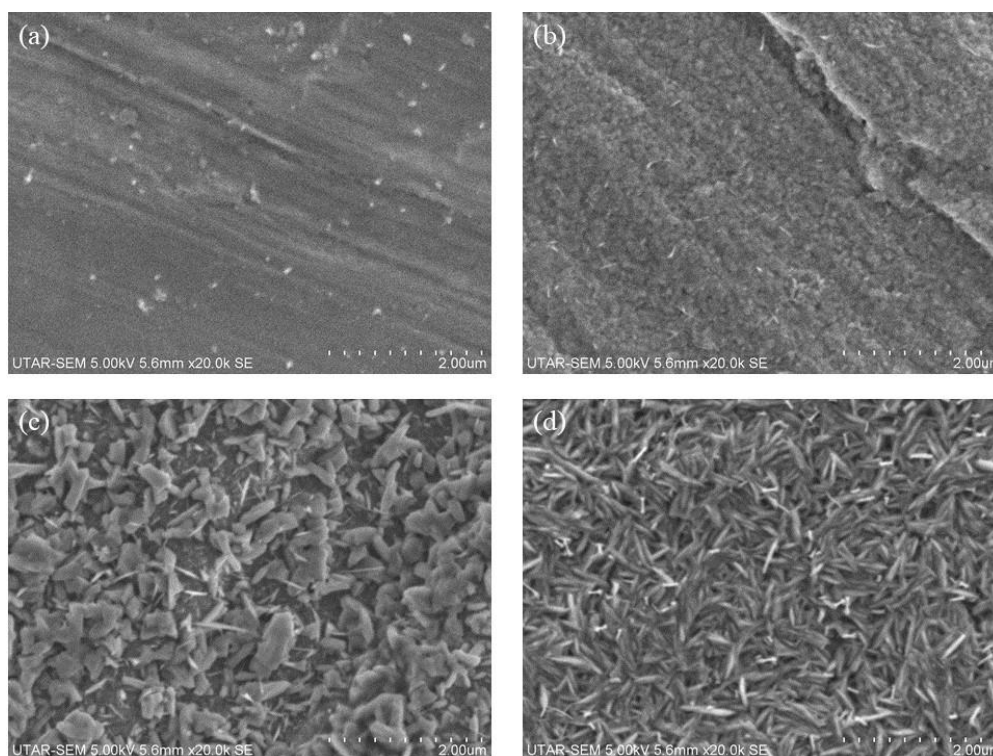


Figure 4.1: SEM Images of Iron Oxide Synthesised by Different Oxidation Temperatures for 2 h: (a) 200, (b) 300, (c) 400, and (d) 500 °C.

By observing Figure 4.1 (a), there was no nanostructures formed on the surface of specimen when the iron foil was oxidised at 200 °C. Only uneven oxide could be seen on the surface of the iron substrate. Similarly, the iron foil oxidised at 300 °C for 2 h shown in Figure 4.1 (b) did not grow significant nanostructures on the surface of iron foil. Thicker oxide layer was formed as compared to the specimen oxidised at 200 °C. When the oxidation temperature of iron foil was increased to 400 °C, it is observed that irregular cloud-like structures of oxide with only scarce and very less amount of nanosheets were grown on the iron substrate as shown in Figure 4.1 (c). The sparse nanosheets formed on the surface were randomly distributed with extremely low areal density. For the iron oxidised at 500 °C as shown in Figure 4.1 (d), it can be clearly seen that densely packed iron oxide nanosheets which covering the surface of the iron foil uniformly were produced. More obvious iron oxide nanosheets were observed as compared to

other samples oxidised at 200, 300, and 400 °C. The nanosheets were observed to be grown significantly with much higher areal density. The width of the nanosheets calculated by the software ImageJ was ranging from 258-696 nm with the thickness of nanosheets ranging from 22-32 nm, while the average width and thickness of the nanosheets were 399 nm and 28 nm, respectively. It was proposed that the formation of uniform nanostructures increases the surface areas to provide more sites for the reduction of Cr (VI) ions which enhances the Cr (VI) removal efficiency of the specimen (Lockman, 2018).

The results shown in Figure 4.1 proves that the oxidation temperatures at 200 and 300 °C were not enough to induce the growth of iron oxide nanostructures. Also, oxidation temperature of 400 °C was insufficient to grow densely packed and uniform iron oxide sheets. However, it was observed that the specimen oxidised at 500 °C produced more uniform nanosheets with higher areal density. It is obvious that there was an evolution of nanostructures formed with increasing oxidation temperature. This can be explained where the oxidation rates were enhanced at higher temperatures due to more diffusion paths for atomic transport of iron and oxygen (Bertrand et al., 2010). The oxidation temperatures were set below 570 °C in this work in order to produce the iron oxide nanostructures with a multilayer of hematite and magnetite (Chen and Yuen, 2003). The iron oxide nanosheets synthesised at 500 °C for 2 h are similar to the nanostructures produced in the work done by Budiman et al. (2016a) and Aquino et al. (2018). Apart from that, one possible hypothesis can be proposed is that at higher oxidation temperatures, the growth of nanostructures with higher areal density can be excited. In short, the iron foil oxidised at 500 °C for 2 h produced the best nanostructures in the form of nanosheets compared to the iron foils oxidised at other temperatures which possessed higher surface area of iron oxide for electrostatic reaction in Cr (VI) removal process (Budiman et al., 2016b).

4.2.2 The Effect of the Oxidation Duration on the Growth of Iron Oxides

According to the result obtained in Section 4.2.1, the sample oxidised at 500 °C for 2 h possessed the best nanostructures in which high uniformity

and areal density of nanosheets was observed. Therefore, to study the effect of oxidation duration on the growth of iron oxides, thermal oxidation of iron foils were conducted at 500 °C for different period including 0.5, 1, 1.5, 2, 2.5, and 3 h. Figure 4.2 shows the SEM images of different specimens synthesised at 500 °C for different duration. All the specimens were observed to be covered uniformly by the nanostructures produced by thermal oxidation at different duration.

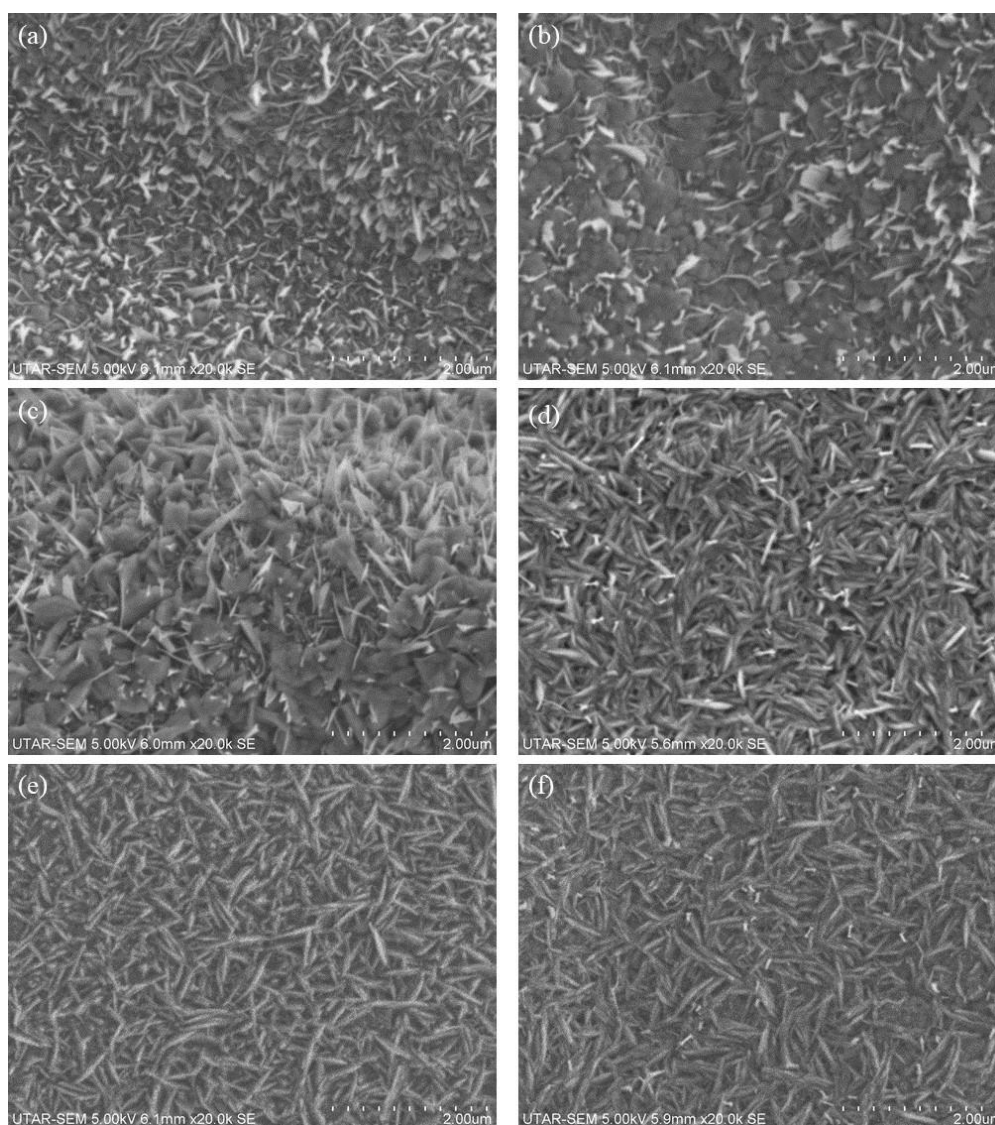


Figure 4.2: SEM Images of Iron Oxide Nanostructures Synthesised at 500 °C for Different Oxidation Time: (a) 0.5, (b) 1, (c) 1.5, (d) 2, (e) 2.5, and (f) 3 h.

Table 4.1 shows the dimensions including the width and thickness of the nanosheets formed on the samples oxidised for duration of 0.5, 1, 1.5, 2, 2.5, and 3 h. Based on the observation in Figure 4.2 (a), the nanosheets produced on the specimen oxidised at 500 °C for 0.5 h was rather short and flat. Flat nanosheets instead of blade-like morphologies were formed on the surface of iron substrate. The width of the nanosheets was ranging from 73-370 nm while the thickness of nanosheet ranged from 16-50 nm. The average width and thickness of iron oxide nanosheets synthesised at 0.5 h oxidation period are 193 nm and 29 nm, respectively. Next, the nanosheets produced at the oxidation period of 1 h has similar structures with the specimen oxidised for 0.5 h, as shown in Figure 4.2 (b). Some blade-like nanosheets were observed. The nanosheets formed was observed to have larger width, ranging from 106-398 nm with the average nanosheets width of 283 nm, whereas the thickness of nanosheets was ranging from 21-47 nm with the average thickness of 31 nm. When the oxidation period was increased to 1.5 h, more significant blade-like nanosheets were formed, as shown in Figure 4.2 (c). The nanosheets was rather tapered where the width at the bottom of nanosheets was larger than at the top. At this duration, the width of the nanosheets produced on the 1.5 h specimen was ranging from 131-592 nm with the average width of 292 nm. Other than that, the thickness of the nanosheets formed was within the range of 15-36 nm, with the average thickness of 27 nm.

Table 4.1: Dimensions of Nanosheets Formed on the Samples Oxidised at 500 °C for Different Duration.

Sample	Width (nm)		Thickness (nm)	
	Range	Average	Range	Average
0.5 h	73-370	193	16-50	29
1.0 h	106-398	283	21-47	31
1.5 h	131-592	292	15-36	27
2.0 h	258-696	399	22-32	28
2.5 h	245-753	473	21-39	30
3.0 h	351-709	510	35-61	44

Besides, Figure 4.2 (d) shows the iron oxide nanosheets synthesised on the specimen oxidised at 500 °C for 2 h, which was discussed previously in Section 4.2.1. The nanosheets grown on the substrate was more obvious and uniform with higher areal density as compared to the nanosheets formed at the oxidation duration of 0.5, 1, and 1.5 h. Densely packed nanosheets was formed, with the width and thickness ranging from 258-696 nm and 22-32 nm, respectively. The nanosheets oxidised for 2 h has the average width of 399 nm and the average thickness of 28 nm. Next, when the oxidation time was prolonged to 2.5 h, even more obvious nanosheets was observed in which the nanosheets formed on the specimen was found to be larger in width and denser. The nanosheets formed on this specimen has the width and thickness ranging from 245-753 nm and 21-39 nm. The average width and thickness of the nanosheets were also determined, which are 473 nm and 30 nm, respectively. When the oxidation duration was increased to 3 h, nanosheets with lesser areal density was observed on the surface of iron foil as shown in Figure 4.2 (f). Similar structures as the specimen oxidised for 2.5 h were produced, but the nanostructures on the iron foil oxidised for 3 h was not as significant and obvious as in 2.5 h specimen. Some nanosheets were found to be thicker which possibly merged with the adjacent nanosheets. The width and thickness of the nanosheets were found in the range of 351-709 nm and 35-61 nm with the average width and thickness of 510 nm and 44 nm, respectively.

The results in Figure 4.2 shows an increment in the average width of iron oxide nanosheets produced on each specimen as the oxidation duration increases from 0.5 to 2.5 h. Meanwhile, the average thickness of the nanosheets formed on each sample did not vary much (within 27-31 nm), except the nanosheets produced at the oxidation duration of 3 h (44 nm). The improvement of nanostructures produced indicates that the oxidation duration plays an crucial role in the formation and enhancement of iron oxide nanosheets. The longer the oxidation duration, the more obvious and significant the nanostructures formed, resulting in higher areal density of nanostructures (Hiralal et al., 2008; Budiman et al., 2016b). However, an interesting phenomenon in which the enhancement of the nanostructures due to increasing oxidation period was not obeyed in the specimen oxidised for 3

h. Contrary to the expectations, the nanosheets formed become less dense and not obvious as compared to previous sample oxidised at 2.5 h. The results obtained with sudden decrease at 3 h in an increasing trend was found different with the assessment done by Budiman et al. (2016b). In their work, much more obvious nanosheets with higher areal density were observed at longer oxidation time. A possible argument can be suggested that at the oxidation duration of 3 h, the nanosheets experienced overgrowth such that one nanosheet merged with the adjacent nanosheets, resulting in thicker pieces of nanostructures and reduced areal density (Rahmat et al., 2020). Hence, it can be concluded that the iron foil oxidised at 2.5 h possessed the best surface morphology of high areal density nanosheets with larger width and fine thickness, which was assumed to be able to provide the highest surface area for the reduction reaction of Cr (VI) ions.

Subsequently, the SEM analysis tilted with 45° was conducted to examine the cross section of the iron oxide synthesised at 500°C for 1.5, 2, 2.5, and 3 h in order to identify the height of nanosheets layer. Figure 4.3 shows the cross sectional SEM images of iron foil oxidised at 1.5, 2, 2.5, and 3 h. The cross sectional SEM images revealed that the oxide layer mainly comprised of 2 layers, where the upper surface layer consisted of $\alpha\text{-Fe}_2\text{O}_3$ (hematite) nanostructures and the inner layer was the columnar grains of Fe_3O_4 (Chen and Yuen, 2003), which denoted as the yellow arrows in Figure 4.3.

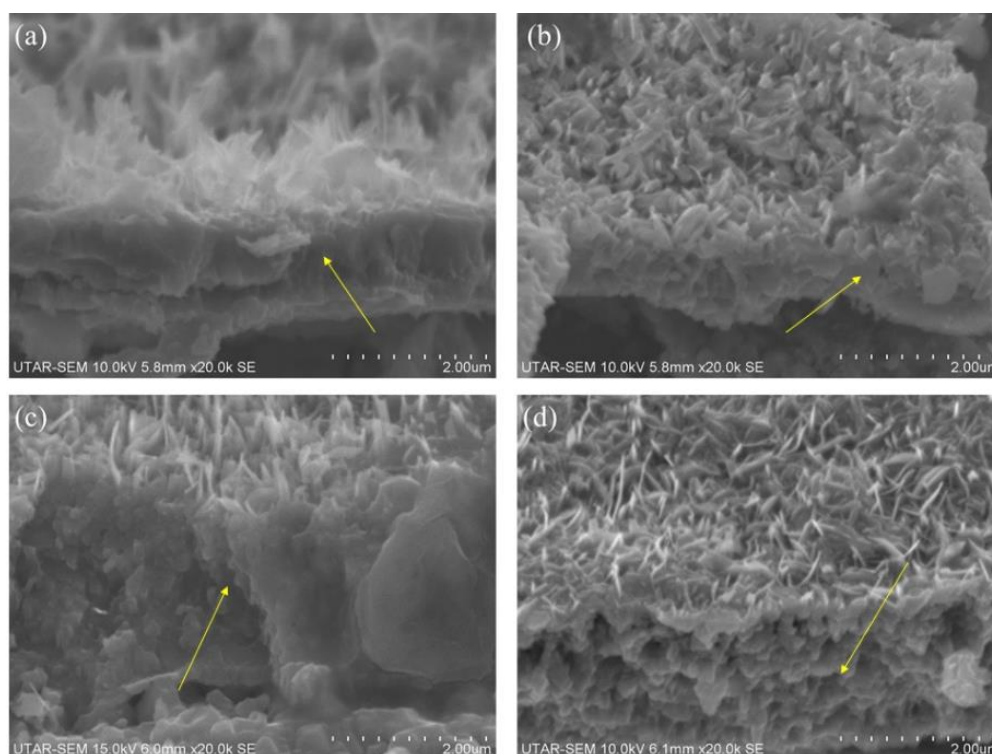


Figure 4.3: The Cross Sectional SEM Images Tilted 45° of the Iron Foil Oxidised at 500°C for (a) 1.5, (b) 2, (c) 2.5, and (d) 3 h.

For the iron foil oxidised for 1.5 h as shown in Figure 4.1 (a), the height of the nanosheets formed was ranging from 473-1079 nm (average of 751 nm). Next, the nanosheets synthesised on the sample oxidised for 2 h shown in Figure 4.3 (b) had a height range within 321-668 nm with the average height of 496 nm. On the other hand, Figure 4.3 (c) shows the cross section of the nanosheets formed on the sample oxidised for 2.5 h, the height of the nanosheets layer ranged from 507-980 nm with the average height of 766 nm. The cross sectional images of iron oxide nanosheets oxidised for 3 h possessed the nanosheets layer with a height of ranging within 207-529 nm, as shown in Figure 4.3 (d). The average height of the nanosheets formed was 366 nm. Table 4.2 summarises the heights of nanosheets formed on the oxide layer of the samples oxidised at 500°C for 1.5, 2, 2.5, and 3 h.

Table 4.2: The Heights of Nanosheets Formed on the Oxide Layer of the Samples Oxidised at 500 °C for 1.5, 2, 2.5, and 3 h.

Sample	Range (nm)	Average (nm)
1.5 h	473-1079	751
2.0 h	321-668	496
2.5 h	507-980	766
3.0 h	207-529	366

The result in Figure 4.3 suggests that iron foil oxidised for 2.5 h at 500 °C produced the nanosheets with the highest average height of the ~766 nm as compared to the specimens synthesised at other different oxidation durations. It is proven that the suggestion proposed based on the results in Figure 4.2 previously which revealed that sample oxidised at 500 °C for 2.5 h possessed the best nanosheets (larger width and high areal density with fine thickness) was acceptable and consistent with the results shown in Figure 4.3. Therefore, from the results obtained in this subsection, it can be deduced that the optimal oxidation duration for the oxidation of iron foil in the presence of potassium iodide powder is 2.5 h. Larger width and greater height of nanosheets with fine thickness and higher areal density were produced on the specimen, which was expected to provide more surface area for the electrostatic reaction.

4.2.3 The Effect of the Presence of Potassium Iodide in Thermal Oxidation on the Growth of Iron Oxide

In this work, thermal oxidation of iron foils were conducted in the presence of potassium iodide (KI) powder. To study the effect of the presence of KI, an iron foil was oxidised at 500 °C for 2 h without KI powder, and it was compared with the sample oxidised under same oxidation parameters with the presence of KI powder. Figure 4.4 shows the SEM images of iron oxide nanosheets formed by thermal oxidation at 500 °C for 2 h: (a) with and (b) without KI powder.

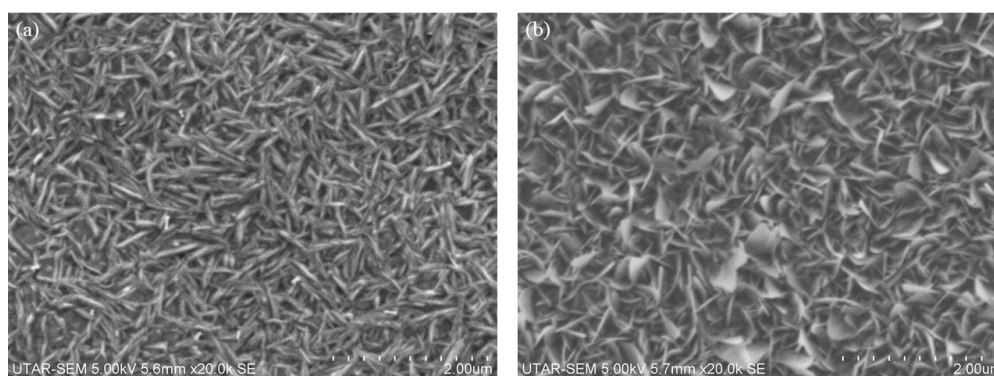


Figure 4.4: SEM Images of Iron Oxide Nanostructures Formed by Thermal Oxidation at 500 °C for 2 h: (a) With and (b) Without KI Powder.

For the sample oxidised at 500 °C for 2 h in the presence of KI powder as shown in Figure 4.4 (a), uniform blade-like nanosheets were observed which discussed previously in Section 4.2.1. Densely packed nanosheets were formed which covered the surface of substrate uniformly. The nanosheets synthesised here has an average height and width of 399 nm and 28 nm. As a comparison, another iron foil was oxidised at same oxidation parameters, but no KI powder covered on the sample in oxidation process. Based on Figure 4.4 (b), it can be seen that flower-like nanosheets instead of blade-like nanosheets were synthesised on the surface of the sample. The nanosheets appeared to be thicker and larger as the width of the nanosheets ranged from 205-573 nm with the thickness of 21-51 nm. The average width and thickness of the nanosheets were 438 nm and 33 nm, respectively.

It was noticed that higher areal density and more uniform nanosheets with finer thickness were observed on the sample oxidised with KI. The results shown in Figure 4.4 proved that the presence of KI in thermal oxidation enhanced the growth of iron oxide nanostructures in which more uniform and finer blade-like nanosheets can be produced on the surface of oxidised sample. This is consistent with the research carried out by Qi, Wang and Liu (2003) which suggested that potassium halide was recommended to be oxidised with metals to enhance the growth of nanostructures. An adequate explanation can be suggested that KI salts produced tiny droplets at the oxidation temperature of 500 °C, which serve as the important templates for nanosheets growth. The iron oxide was then dissolved in the tiny droplets

and reached supersaturating state to form potassium-doped iron oxide nanosheets.

An interesting finding in this work is that the nanostructures formed in this work was nanosheets instead of nanowires. A possible mechanism was proposed by Budiman et al. (2016a), suggesting that the formation of nanosheets was based on the transformation of existing nanowires to nanosheets. It was expected that the diffusion rate led to the lateral growth on the side wall of nanostructures was faster than the central core diffusion rate. Nevertheless, nanowires must be firstly developed in order to transform into the blade-like nanosheets (Budiman et al., 2016a; 2016b). In short, it can be concluded that the presence of KI powder in the oxidation of iron foil was essential in enhancing the growth of iron oxide nanosheets.

4.3 Structural Analysis: X-Ray Diffraction (XRD)

XRD analysis was conducted on the specimen oxidised with potassium iodide (KI) at 500 °C for the oxidation duration of 0.5, 1, 1.5, 2, 2.5, and 3 h to examine the existing phases in the specimens. Bare iron foil was analysed as a reference while the sample oxidised at 500 °C for 2 h without KI was investigated as well to compare the XRD peaks with the sample oxidised with KI under same oxidation parameters. Figure 4.5 shows the XRD patterns of bare iron foil, iron foils oxidised with KI powder at 500 °C for duration of 0.5, 1, 1.5, 2, 2.5, and 3h, and the iron foil oxidised without KI powder at 500 °C for 2 h.

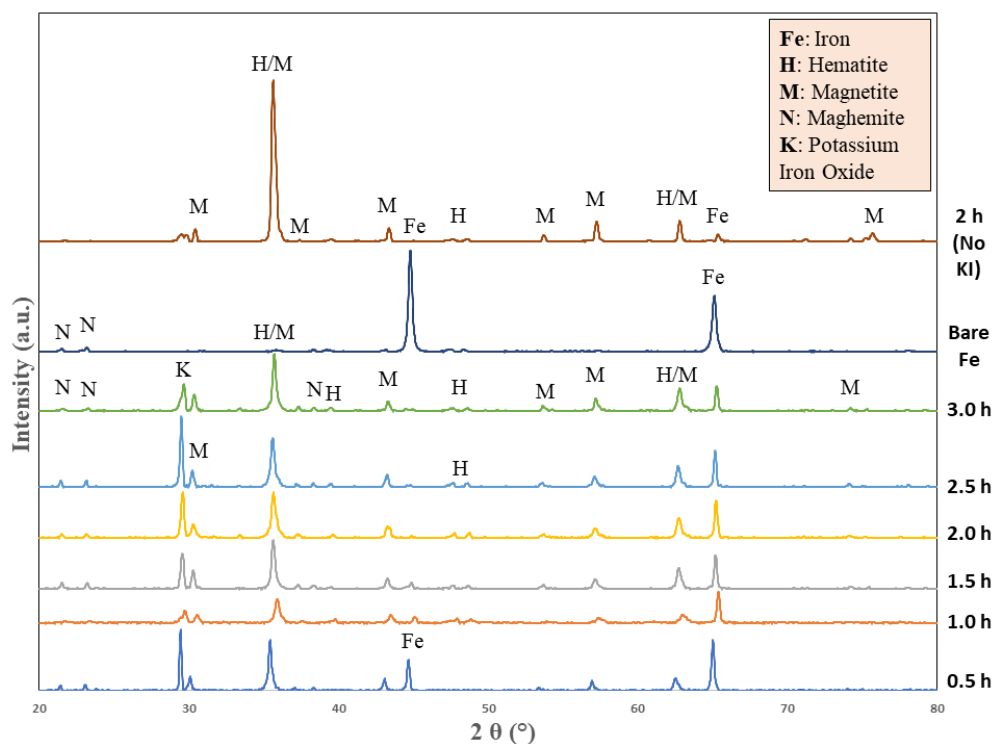


Figure 4.5: XRD Patterns of Bare Fe Foil, Iron Foils Oxidised with KI Powder at 500 °C for Duration of 0.5, 1, 1.5, 2, 2.5, and 3 h, and the Iron Foil Oxidised at 500 °C for 2 h Without KI powder.

XRD pattern of the bare Fe foil displayed 2 distinct peaks at 44.8° and 65.1° in the orientation of (110) and (200), respectively, which are indexed to ICDD: 006-0696 that representing cubic Fe. Besides, 3 small peaks were observed at 21.52° (201), 23.16° (115) and 38.32° (209) on the bare foil and some other samples which matching with maghemite indexed to ICDD: 015-0615. This may be due to the existing layer of oxide layer on the iron substrate. For most of the samples oxidised in the presence of KI powder, similar peaks had been observed with different intensities and multiple oxide phases had been identified, including hematite, magnetite, maghemite, and potassium-doped iron oxide. First, for the samples oxidised for 0.5-2.5 h, the most dominant peak which possessed the highest intensity was observed at 29.5° at the orientation of (013) indicating the presence of orthorhombic potassium doped iron oxide, K_2FeO_4 indexed to ICDD: 025-0652 due to existing KI powder on the iron substrate during oxidation. Cubic magnetite (Fe_3O_4) phase was also existing at the peaks found at 30.2° (220), 37.16°

(222), 43.24° (400), 53.6° (422), 57.1° (511), and 74.12° (533) which indexed to ICDD: 001-1111 and 065-0731. Other than that, distinct peaks that indicating the phases of rhombohedral hematite and cubic magnetite are identified at 35.6° (110; 311) and 62.68° (214; 440), which is consistent with previous works that proposed the existence of multilayered oxide comprised of thin hematite layer and thick magnetite (Chen and Yuen, 2003; Budiman et al., 2016b; Aquino et al., 2018).

By comparing the samples oxidised in the presence of potassium iodide powder, the XRD patterns showed that the iron foil oxidised for 2.5 h possessed the highest intensities in most peaks, indicating that the sample was highly crystallised. As mentioned, the most dominant peak was identified, which is matched with the potassium iron oxide, K_2FeO_4 . This proves the growth of highly crystallised potassium-doped iron oxide nanosheets. On the other hand, the decrease observed in intensities of XRD peaks of 3 h sample further proved that the sample has lower degree of crystallinity. The peak attributed to K_2FeO_4 shown in the 3 h sample significantly reduced, and the dominant peak in this sample was replaced by the phases consisted of hematite and magnetite. From the result, it can be deduced that the sample oxidised in the presence of potassium iodide achieved the highest degree of crystallinity with the dominant phase of K_2FeO_4 at 2.5 h of oxidation duration. When the oxidation was prolonged to 3 h, the oxide becomes less crystallised with dominant peak attributed to phases of hematite and magnetite. It is consistent with the results obtained from SEM analysis in Section 4.2 which agrees to 2.5 h as the optimum oxidation duration for better iron oxide nanosheets growth.

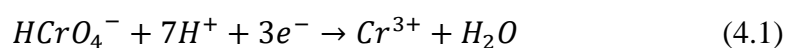
The sample oxidised at $500^\circ C$ for 2 h without KI powder was examined by XRD analysis to study the effect of KI to the phases of oxide formed. From the XRD pattern, oxidation without KI produced the oxide layer mainly consisted of hematite and magnetite. Distinct peak of hematite (110) and magnetite (311) at 35.62° was the most dominant peak which indicates highly crystallised oxides comprised of hematite and magnetite was synthesised in this sample. Other peaks which matched with the magnetite phase denoted as M in Figure 4.5 were found similar to samples discussed above. The XRD pattern of the sample is consistent with work done by Chen

and Yuen (2002). The result shows that no potassium-doped iron oxide phase was identified as compared to other samples oxidised in the presence of KI. Apart from that, it can be concluded that the presence of KI in the oxidation of iron foil induced the growth of potassium-doped iron oxide nanosheets.

4.4 Chromium (VI) Removal Analysis

In this section, Cr (VI) removal tests were carried out on various specimens including the samples oxidised at 500 °C for the duration of 0.5, 1, 1.5, 2, 2.5, and 3 h in the presence of KI powder, and bare iron foil as the reference measurement for the removal efficiency. Besides, the sample oxidised at 500 °C for 2 h without KI was tested as well to compare the Cr (VI) removal efficiency of both sample under same oxidation parameters.

The process of Cr (VI) removal occurs based on the mechanism of Cr (VI) ions reduction by the iron oxide samples as the adsorbents. The Cr (VI) ions in the chromium solution tuned at pH 2 exist in the form of negatively charged hydrogen chromate ions (HCrO_4^-) (Budiman et al., 2016b). As the oxidised sample was put into the Cr (VI) solution in the conical flask, the surface charge of the nanosheets was protonated to be positively charged due to the proton (H^+) supplied in the acidic aqueous solution. Thus, the electrostatic reaction takes place due to the attraction force of negatively charged bichromate ions by the positively charged ions possessed by the iron oxide nanosheets (Budiman et al., 2016b; Lockman, 2018). This leads to the removal of Cr (VI) ions in the aqueous solution. The reduction reaction of Cr (VI) ions is shown in Equation 4.1. Figure 4.6 shows the Cr (VI) removal efficiency of bare Fe foil, iron foils oxidised with KI powder at 500 °C for duration of 0.5, 1, 1.5, 2, 2.5, and 3h, and the iron foil oxidised at 500 °C for 2 h without KI powder in 30 min.



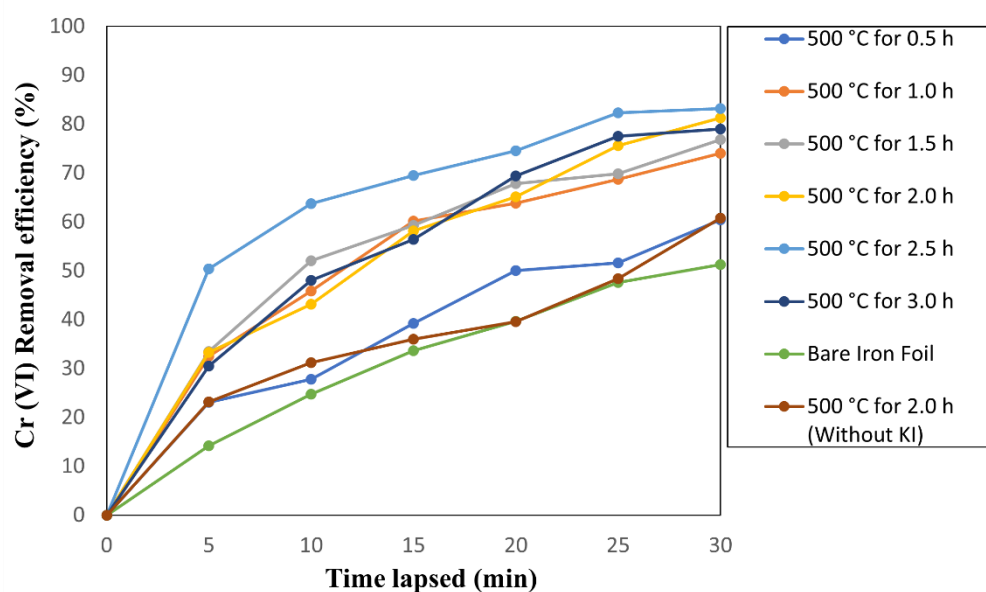


Figure 4.6: Cr (VI) Removal Efficiency of Bare Fe Foil, Iron Foils Oxidised with KI Powder at 500 °C for Duration of 0.5, 1, 1.5, 2, 2.5, and 3 h, and the Iron Foil Oxidised at 500 °C for 2 h Without KI Powder in 30 min.

Based on the results shown in Figure 4.5, bare iron foil has the lowest Cr (VI) removal efficiency of 51.22 % among the sample tested. For the sample oxidised at 500 °C with KI, the Cr (VI) removal efficiency of 0.5, 1, 1.5, 2, 2.5, and 3 h samples were determined, which are 60.40, 74.05, 76.84, 81.29, 83.22, and 79.01 %, respectively. The results showed an increasing trend of removal efficiency in the samples of 0.5-2.5 h. Meanwhile, as the oxidation duration was increased to 3 h, it was observed that the Cr (VI) removal efficiency of the sample dropped to 79.01 % which opposed to the result trend of previous samples. From the result obtained, it was noticed that the 2.5 h sample generated the best performance in removing Cr (VI) ions, which providing the highest removal efficiency of 83.22 % as presented in Figure 4.5. This removal efficiency is higher than the result obtained by Budiman et al. (2016a) in which iron oxide nanosheets produced by thermal oxidation in water vapour has the Cr (VI) removal efficiency lower than 80 % at 30 min in 50 ml of 10 mg/L Cr (VI) solution. Apart from that, it is possible to speculate that oxidation of iron foil in the presence of potassium iodide is

more efficient than that in water vapour, which proves the effectiveness of potassium iodide as the alternative approach in the oxidation of iron.

Besides, the Cr (VI) removal test results further verified the inference proposed in Section 4.2.2, which suggested 500 °C and 2.5 h as the optimum oxidation temperature and duration, respectively. This can be correlated to the surface morphology of the 2.5 h sample which possessed high areal density of nanosheets with larger width and rather fine thickness as compared to other oxidised samples. This resulted to larger effective surface areas which provided more sites for the reduction reaction to occur. Furthermore, the samples produced by thermal oxidation at 500 °C for 2 h with and without KI powder were compared as well. Figure 4.6 revealed that the Cr (VI) removal efficiency of the sample oxidised with KI was higher than the one oxidised without KI, which are 81.29 % and 60.77 %, respectively. The results appear to confirm that the presence of KI powder in the oxidation of iron foil enhanced the Cr (VI) removal efficiency.

In short, iron foil oxidised at 500 °C for 2.5 h in the presence of KI powder has the best Cr (VI) removal efficiency of 83.22 % in 30 min. From the results obtained, it is concluded that Cr (VI) removal efficiency of the samples oxidised is mainly affected by the surface morphology of the nanosheets produced on the iron substrate. Therefore, to improve the Cr (VI) removal efficiency, it is crucial to increase surface area of the iron oxide, where more effective sites will be involved in the electrostatic reaction with Cr (VI) ions for removal purposes. Other than that, the oxidation process of the iron foil is strongly suggested to be conducted in the oxygen-rich environment to enhance the growth of iron oxide nanosheets with better surface morphology.

4.5 Summary

In this chapter, the optimum oxidation temperature and duration for the synthesis of iron oxide nanosheets in the presence of potassium iodide (KI) were determined by the sample characterisation tests. According to the SEM analysis, the nanosheets formed on the surface of the iron foil oxidised at 500 °C for 2.5 h was observed to have higher areal density and average height of 766 nm with fine thickness (averagely 30 nm) which possessed

larger surface area to provide more sites on the surface for Cr (VI) removal. From the XRD analysis, various phases of oxides were determined on the oxidised samples including hematite (ICDD: 033-0664), magnetite (ICDD:001-1111 and 065-0731) and potassium iron oxide, K_2FeO_4 (ICDD: 025-0652). The sample oxidised at 500 °C for 2.5 h was observed to have the highest intensities of XRD peaks in overall among the samples, indicating that the oxides formed were highly crystallised. Last but not least, the Cr (VI) removal test shows that iron oxidised 500 °C for 2.5 h in the presence of KI powder achieved the highest removal efficiency of 83.22 % in 30 min. It was found that the existence of iron oxide nanosheets enhanced the Cr (VI) removal efficiency as compared to the bare Fe foil.

CHAPTER 5

CONCLUSIONS AND RECOMMENDATIONS

5.1 Conclusions

In conclusion, thermal oxidation of the iron oxide in the presence of potassium iodide (KI) successfully synthesised the iron oxide nanosheets. The aim and objectives of this project were achieved. Optimum oxidation parameters such as temperature and holding time of oxidation process to grow iron oxide nanosheets were identified, which are 500 °C and 2.5 h. Based on the SEM images, the iron oxide nanosheets formed in the sample oxidised at 500 °C for 2.5 h in the presence of KI powder has higher areal density and larger width with rather fine thickness. The average dimensions including nanosheets width, height and thickness were calculated, which are 473, 766, and 30 nm, respectively. It is possible to speculate that the nanosheets formed at optimum parameters possessed larger surface area which provided more sites for electrostatic reaction in chromium removing process, thus enhancing the oxide Cr (VI) removal efficiency. In addition, the presence of KI powder in the oxidation of iron foil enhanced the surface morphology of the sample, forming blade-like nanosheets with finer thickness instead of flower-like nanosheets as shown in the SEM image of the sample oxidised at similar oxidation parameters without potassium iodide.

The XRD analysis revealed that various oxides were identified on the sample oxidised with KI, including hematite, magnetite, and the dominant peak of potassium iron oxide, K_2FeO_4 . The sample oxidised with KI powder at 500 °C for 2.5 h showed the highest intensities in overall as compared to other samples in the XRD patterns, indicating that 2.5 h sample was highly crystallised. Last but not least, the results shown in Cr (VI) removal test indicates that the sample oxidised at 500 °C for 2.5 h with KI achieved the best removal efficiency of 83.22 % among the samples tested in 30 min.

In short, the results obtained from this work proved the success of synthesising iron oxide nanosheets by thermal oxidation with KI powder. Suitable oxidation temperature and duration are necessarily required to grow

the iron oxide with good surface morphology and high degree of crystallinity in order to provide excellent performance in removing Cr (VI) ions.

5.2 Recommendations for future work

Throughout the research project, several recommendations are suggested to be implemented in future work. In this work, potassium iodide (KI) was used as the catalyst in the oxidation of iron foil in dry air. The replacement of KI as the K-compound with potassium hydroxide (KOH) is definitely worth to be studied in future as there were previous works done on the thermal oxidation of other metals with KOH at similar temperature.

Next, during the preparation of samples in the SEM analysis tilted with 45 °, it was found that the sample oxidised was not easy to be torn by hands due to the behaviour of iron oxide foils. Cutting of the samples using cutter was not suggested since the cutting force could damage the nanostructures formed on the sample from the cross-sectional view. Hence, a suggestion is proposed that the oxide sample can be mixed with liquid nitrogen to freeze the metal oxide sample. Cryogenic hardening on the sample allows easier tearing of the oxide foils.

Moreover, it was observed that the layer of iron oxide foils were delaminated during Cr (VI) removal test. Therefore, the sample of chromium solution during the Cr (VI) removal test must be collected carefully so that no delaminated oxides will be collected together into the centrifugal tube, causing the results of UV-Vis test to be affected.

REFERENCES

- Aigbe, U.O. and Osibote, O.A., 2020. A review of hexavalent chromium removal from aqueous solutions by sorption technique using nanomaterials. *Journal of Environmental Chemical Engineering*, 8(6), p.104503.
- Aquino, C.L.E., Bongar, M.J.C., Silvestre, A.B. and Balela, M.D.L., 2018. Synthesis of hematite (α -Fe₂O₃) nanostructures by thermal oxidation of iron sheet for Cr (VI) adsorption. *Key Engineering Materials*, KEM 775, pp.395–401.
- Ashraf, M., Khan, I., Usman, M., Khan, A., Shah, S.S., Khan, A.Z., Saeed, K., Yaseen, M., Ehsan, M.F., Tahir, M.N. and Ullah, N., 2020. Hematite and magnetite nanostructures for green and sustainable energy harnessing and environmental pollution control: A review. *Chemical Research in Toxicology*, 33(6), pp.1292–1311.
- Bertrand, N., Desgranges, C., Poquillon, D., Lafont, M.C. and Monceau, D., 2010. Iron oxidation at low temperature (260-500 °C) in air and the effect of water vapor. *Oxidation of Metals*, 73(1), pp.139–162.
- Budiman, F., Bashiro, N., Tan, W.K., Razak, K.A., Matsuda, A. and Lockman, Z., 2016a. Rapid nanosheets and nanowires formation by thermal oxidation of iron in water vapour and their applications as Cr (VI) adsorbent. *Applied Surface Science*, 380, pp.172–177.
- Budiman, F., Tan, W.K., Razak, K.A., Atsunori, M. and Lockman, Z., 2016b. The assessment of Cr (VI) removal by iron oxide nanosheets and nanowires synthesized by thermal oxidation of iron in water vapour. *Procedia Chemistry*, 19, pp.586–593.
- Burks, T., Avila, M., Akhtar, F., Göthelid, M., Lansåker, P.C., Toprak, M.S., Muhammed, M. and Uheida, A., 2014. Studies on the adsorption of chromium(VI) onto 3-mercaptopropionic acid coated superparamagnetic iron oxide nanoparticles. *Journal of Colloid and Interface Science*, 425, pp.36–43.
- Chen, D., Xiong, S., Ran, S.H., Liu, B., Wang, L.M. and Shen, G.Z., 2011. One-dimensional iron oxides nanostructures. *Science China Physics, Mechanics & Astronomy*, 54(7), pp.1190–1199.
- Chen, R.Y. and Yuen, W.Y.D., 2003. Review of the high-temperature oxidation of iron and carbon steels in air or oxygen. *Oxidation of Metals*, 59(5), pp.433–468.
- Chew, B.K., Jun, H.K., Lockman, Z., Razak, K.A. and Ng, C.Y., 2019. Hydrothermal growth of Fe₂O₃ nano/micro-rods on Fe foil for Cr (VI) removal. *Materials Today: Proceedings*, 17(3), pp.1018–1023.

Cornell, R.M. and Schwertmann, U., 2003. *The iron oxides: structures, properties, reactions, occurrences and uses*. Second, Co ed. John Wiley & Sons, 2003.

Ding, Y. and Wang, Z.L., 2004. Structure analysis of nanowires and nanobelts by Transmission Electron Microscopy. *The Journal of Physical Chemistry B*, 108(33), pp.12280–12291.

Feng, X., Yu, Z., Sun, Y., Long, R., Shan, M., Li, X., Liu, Y. and Liu, J., 2021. Review MXenes as a new type of nanomaterial for environmental applications in the photocatalytic degradation of water pollutants. *Ceramics International*, 47(6), pp.7321–7343.

Fu, Y.Y., Wang, R.M., Xu, J., Chen, J., Yan, Y., Narlikar, A. v. and Zhang, H., 2003. Synthesis of large arrays of aligned α -Fe₂O₃ nanowires. *Chemical Physics Letters*, 379(3–4), pp.373–379.

Galán, B., Castañeda, D. and Ortiz, I., 2005. Removal and recovery of Cr(VI) from polluted ground waters: A comparative study of ion-exchange technologies. *Water Research*, 39(18), pp.4317–4324.

Grigorescu, S., Lee, C., Lee, K., Albu, S., Paramasivam, I., Demetrescu, I. and Schmuki, P., 2012. Thermal air oxidation of Fe: Rapid hematite nanowire growth and photoelectrochemical water splitting performance. *Electrochemistry Communications*, 23, pp.59–62.

Han, Q., Xu, Y.Y., Fu, Y.Y., Zhang, H., Wang, R.M., Wang, T.M. and Chen, Z.Y., 2006. Defects and growing mechanisms of α -Fe₂O₃ nanowires. *Chemical Physics Letters*, 431(1–3), pp.100–103.

Hedayatnasab, Z., Abnisa, F. and Daud, W.M.A.W., 2017. Review on magnetic nanoparticles for magnetic nanofluid hyperthermia application. *Materials & Design*, 123, pp.174–196.

Hiemstra, T., 2018. Surface structure controlling nanoparticle behavior: Magnetism of ferrihydrite, magnetite, and maghemite. *Environmental Science: Nano*, 5(3), pp.752–764.

Hiralal, P., Saremi-Yarahmadi, S., Bayer, B.C., Wang, H., Hofmann, S., Upul Wijayantha, K.G. and Amaratunga, G.A.J., 2011. Nanostructured hematite photoelectrochemical electrodes prepared by the low temperature thermal oxidation of iron. *Solar Energy Materials and Solar Cells*, 95(7), pp.1819–1825.

Hiralal, P., Unalan, H.E., Wijayantha, K.G.U., Kursumovic, A., Jefferson, D., MacManus-Driscoll, J.L. and Amaratunga, G.A.J., 2008. Growth and process conditions of aligned and patternable films of iron (III) oxide nanowires by thermal oxidation of iron. *Nanotechnology*, 19(45), p.455608.

Hsu, L.C., Li, Y.Y., Lo, C.G., Huang, C.W. and Chern, G., 2008. Thermal growth and magnetic characterization of α -Fe₂O₃ nanowires. *Journal of Physics D: Applied Physics*, 41(18), p.185003.

Kerur, S.S., Bandekar, S., Hanagadakar, M.S., Nandi, S.S., Ratnamala, G.M. and Hegde, P.G., 2021. Removal of hexavalent chromium-industry treated water and wastewater: A review. *Materials Today: Proceedings*, 42(2), pp.1112–1121.

Kotasâ, J. and Stasicka, Z., 2000. Chromium occurrence in the environment and methods of its speciation. *Environmental Pollution*, 107(3), pp.263–283.
Leonel, A.G., Mansur, A.A.P. and Mansur, H.S., 2021. Advanced functional nanostructures based on magnetic iron oxide nanomaterials for water remediation: A review. *Water Research*, 190, p.116693.

Leonel, A.G., Mansur, H.S., Mansur, A.A.P., Caires, A., Carvalho, S.M., Krambrock, K., Outon, L.E.F. and Ardisson, J.D., 2019. Synthesis and characterization of iron oxide nanoparticles/carboxymethyl cellulose core-shell nanohybrids for killing cancer cells in vitro. *International Journal of Biological Macromolecules*, 132, pp.677–691.

Liu, Z.W., Zhong, M.L. and Tang, C.M., 2013. Large-scale oxide nanostructures grown by thermal oxidation. *IOP Conference Series Materials Science and Engineering*, 60(1).

Lockman, Z., 2018. *1-dimensional metal oxide nanostructures: Growth, properties, and devices*.

M. K. Chen and K. Olukotun, 2003. The Jrpm system for dynamically parallelizing Java programs. In: *30th Annual International Symposium on Computer Architecture, 2003. Proceedings*. pp.434–445.

Malwal, D. and Packirisamy, G., 2018. Recent advances in the synthesis of metal oxide (MO) nanostructures. In: *Synthesis of Inorganic Nanomaterials*. Elsevier Ltd. pp.255–281.

Qi, H., Wang, C. and Liu, J., 2003. A simple method for the synthesis of highly oriented potassium-doped tungsten oxide nanowires. *Advanced Materials*, 15(5), pp.411–414.

Rafatullah, M., Sulaiman, O., Hashim, R. and Ahmad, A., 2010. Adsorption of methylene blue on low-cost adsorbents: A review. *Journal of Hazardous Materials*, 177(1–3), pp.70–80.

Rahmat, S.T., Tan, W.K., Kawamura, G., Matsuda, A. and Lockman, Z., 2020. Synthesis of rutile TiO₂ nanowires by thermal oxidation of titanium in the presence of KOH and their ability to photoreduce Cr(VI) ions. *Journal of Alloys and Compounds*, 812, p.152094.

Rajeswari, T.R., 2014. Impact of heavy metals on environmental pollution. *Journal of Chemical and Pharmaceutical Sciences*, (3), pp.175–181.

Ramimoghadam, D., Bagheri, S. and Hamid, S.B.A., 2014. Progress in electrochemical synthesis of magnetic iron oxide nanoparticles. *Journal of Magnetism and Magnetic Materials*, 368, pp.207–229.

Rowbotham, A.L., Levy, L.S. and Shuker, L.K., 2000. Chromium in the environment: An evaluation of exposure of the UK general population and possible adverse health effects. *Journal of Toxicology and Environmental Health - Part B: Critical Reviews*, 3(3), pp.145–178.

Sawada, A., Mori, K.I., Tanaka, S., Fukushima, M. and Tatsumi, K., 2004. Removal of Cr (VI) from contaminated soil by electrokinetic remediation. *Waste Management*, 24(5), pp.483–490.

Schwertmann, U. and Cornell, R.M., 2000. *Iron oxides in the laboratory preparation and characterization*.

Shanker, A.K. and Venkateswarlu, B., 2019. Chromium: Environmental pollution, health effects and mode of action. *Encyclopedia of Environmental Health*, pp.650–659.

Sharma, N., Sodhi, K.K., Kumar, M. and Singh, D.K., 2021. Heavy metal pollution: Insights into chromium eco-toxicity and recent advancement in its remediation. *Environmental Nanotechnology, Monitoring and Management*, 15(2), p.100388.

Srivastava, H., Tiwari, P., Srivastava, A.K. and Nandedkar, R. v, 2007. Growth and characterization of Fe₂O₃ nanowires. *Journal of Applied Physics*, 102(5), pp.1–5.

Srivastava, H., Tiwari, P., Srivastava, A.K., Rai, S., Ganguli, T. and Deb, S.K., 2011. Effect of substrate texture on the growth of hematite nanowires. *Applied Surface Science*, 258(1), pp.494–500.

Suman, Devi, S., Sharma, V., Chahal, S., Goel, P., Singh, S., Kumar, A. and Kumar, P., 2021. Phase transformation and structural evolution in iron oxide nanostructures. *Materials Science and Engineering: B*, 272, p.115329.

Sun, H., Brocato, J. and Costa, M., 2015. *Oral chromium exposure and toxicity. Current Environmental Health Reports*,

Takagi, R., 1957. Growth of oxide whiskers on metals at high temperature. *Journal of the Physical Society of Japan*, 12(11), pp.1212–1218.

Ukhurebor, K.E., Aigbe, U.O., Onyancha, R.B., Nwankwo, W., Osibote, O.A., Paumo, H.K., Ama, O.M., Adetunji, C.O. and Siloko, I.U., 2021. Effect of hexavalent chromium on the environment and removal techniques: A review. *Journal of Environmental Management*, 280(111809), pp.1–25.

Vincent, T., Gross, M., Dotan, H. and Rothschild, A., 2011. Thermally oxidized iron oxide nanoarchitectures for hydrogen production by solar-induced water splitting. *International Journal of Hydrogen Energy*, 37(9), pp.8102–8109.

Voss, D.A., Butler, E.P. and Mitchell, T.E., 1982. The growth of hematite blades during the high temperature oxidation of iron. *Metallurgical and Materials Transactions A*, 13(5), pp.929–935.

Wang, R., Chen, Y., Fu, Y., Zhang, H. and Kisielowski, C., 2005. Bicrystalline hematite nanowires. *The Journal of Physical Chemistry B*, 109(25), pp.12245–12249.

Wen, X., Wang, S., Ding, Y., Wang, Z.L. and Yang, S., 2005. Controlled growth of large-area, uniform, vertically aligned arrays of α -Fe₂O₃ nanobelts and nanowires. *The Journal of Physical Chemistry B*, 109(1), pp.215–220.

Wu, W., Wu, Z., Yu, T., Jiang, C. and Kim, W.S., 2015. Recent progress on magnetic iron oxide nanoparticles: Synthesis, surface functional strategies and biomedical applications. *Science and Technology of Advanced Materials*, 16(2).

Yuan, J., Wang, W., Zhu, S. and Wang, F., 2013. Comparison between the oxidation of iron in oxygen and in steam at 650–750 °C. *Corrosion Science*, 75(10), pp.309–317.

Yuan, L., Jiang, Q., Wang, J. and Zhou, G., 2012a. The growth of hematite nanobelts and nanowires-tune the shape via oxygen gas pressure. *Journal of Materials Research*, 27(7), pp.1014–1021.

Yuan, L., Wang, Y., Cai, R., Jiang, Q., Wang, J., Li, B., Sharma, A. and Zhou, G., 2012b. The origin of hematite nanowire growth during the thermal oxidation of iron. *Materials Science and Engineering B*, 177(3), pp.327–336.

Zayed, A.M. and Terry, N., 2003. Chromium in the environment: Factors affecting biological remediation. *Plant and Soil*, 249(1), pp.139–156.

Zhao, C.X., Li, Y.F., Zhou, J., Li, L.Y., Deng, S.Z., Xu, N.S. and Chen, J., 2013. Large-scale synthesis of bicrystalline ZnO nanowire arrays by thermal oxidation of zinc film: Growth mechanism and high-performance field emission. *Crystal Growth & Design*, 13(7), pp.2897–2905.

Zhong, M., Liu, Z., Zhong, X., Yu, H. and Zeng, D., 2011. Thermal growth and nanomagnetism of the quasi-one dimensional iron oxide. *Journal of Materials Science & Technology*, 27(11), pp.985–990.